

OGCM sensitivity experiments on the annual cycle of Western Hemisphere Warm Pool

S.-K. Lee¹, D. B. Enfield² and C. Wang²

¹ Cooperative Institute for Marine and Atmospheric Studies, University of Miami, Miami FL

² Atlantic Oceanographic and Meteorological Laboratory, NOAA, Miami FL

Submitted to *Journal of Geophysical Research (Oceans)*

January 2005 (revised)

ABSTRACT

A series of ocean general circulation (OGCM) model experiments is carried out using the Hybrid Coordinate Ocean Model (HYCOM) to determine the annual cycle of Western Hemisphere Warm Pool (WHWP) heat budget and to assess the appropriateness of commonly used surface flux data sets in driving HYCOM simulations of the WHWP. Among the eight surface heat flux data sets addressed in this study, we find that the simulated SST is closest to the observations when the Southampton constrained (SHC) heat flux data are used, consistent with the conclusion of the data-based study of *Enfield and Lee* [2005]. A preliminary heat budget analysis suggests that the surface net heat flux serves as the dominant forcing mechanism in the WHWP regions except in the equatorial Atlantic where advective processes associated with the equatorial cold tongue are more important. A process of winter overturning that warms the upper layer by convection marks the Gulf of Mexico, while horizontal advection is of little importance there. The eastern north Pacific and Caribbean are affected significantly by vertical and horizontal advection during the onset and peak phases, slowing down the warming considerably. Additional numerical experiments are carried out to explore the sensitivity of the simulated WHWP to different choices of light attenuation and turbulent diffusion models. A marginal but not critical improvement is found by decreasing the average light attenuation depth from 23m (Jerlov type-I) to 17m (Jerlov type-III). For reasonable variations of the critical Richardson number in two different mixing models, there is no significant impact on the results.

1. Introduction

The Western Hemisphere Warm Pool (WHWP) is a body of warm surface water ($\geq 27.5^{\circ}\text{C}$) that develops in the eastern north Pacific (ENP) and the equatorial Atlantic (EQA) between March and June, in the Gulf of Mexico (GoM) between July and August and achieves its maximum size centered over the Caribbean Sea (CBN) between August and [Wang and Enfield, 2001]. In the boreal summer, the WHWP serves as the seasonal convective heating source for the Walker and Hadley circulations in the Western Hemisphere supplying a massive amount of moisture to the atmosphere [Wang and Enfield, 2003, WE03 hereafter], thus affecting the rainfall over the continental United States and Central America [Bosilovich, 2002].

The WHWP is characterized by its large interannual fluctuations in size, which are frequently associated with El Niño-Southern Oscillation (ENSO) and possibly also with the variability internal to the North Atlantic sector [Wang and Enfield, 2001]. According to observations [e.g., Enfield and Mayer, 1996; Klein *et al.*, 1999] and model studies [e.g., Alexander and Scott, 2002], the ENSO-induced reduction of easterlies during the boreal winter (thereby reducing latent heat loss from the ocean) supports a subsequent warming of the tropical North Atlantic and CBN in the boreal spring and summer following the ENSO year. However, during the winter forcing period the subtropical North Atlantic and GoM undergo a cooling due to the strength and unusual southward penetration of frontal passages (thereby increasing latent heat loss). The Pacific North American (PNA) pattern and the Walker/Hadley circulations are the primary processes involved in the Pacific-to-Atlantic ENSO teleconnection [Wang, 2002, 2004; Wang and Enfield, 2003]. To better understand the potential role of the WHWP and its significance in the global-scale climate variability, the first step is to describe the annual cycle of the WHWP, and the involved atmosphere-ocean processes. WE03 initiated this effort by diagnosing the

seasonal variations of the WHWP heat budget, and found that the surface heat flux is mainly responsible for the seasonal cycle of WHWP. *Enfield and Lee* [2004, EL05 hereafter] further refined the work of WE03 by exploring the heat budget of the WHWP using seven surface flux products widely used in climate studies. Through careful analysis by using two approaches to the heat equation, large uncertainties in the surface heat flux products were narrowed down, and the heat flux terms responsible for the development and decay of the four WHWP subregions, namely ENP, GoM, CBN and EQA, were identified. EL05 also found that the contributions by turbulent diffusive heat flux and oceanic advection in the WHWP heat budget are in the range between -2 and -20W/m^2 ($\pm 5\text{W/m}^2$).

The observational analysis of EL05 is constrained to treating the warm pool heat budget in a spatially integrated manner and obtains ocean fluxes indirectly through heat equation residuals. Moreover, the EL05 approach requires considering a warm pool volume as being defined by an isotherm (bubble) and in some months the bubble is nonexistent or too small for analysis, thus critical phases in the development and decay of the warm pool are hindered. In order to overcome these limitations, the work of EL05 is extended here using the HYbrid Coordinate Ocean Model (HYCOM). We have three main objectives in this study. First, by extending the data-based study of EL05 using HYCOM, we wish to see if their conclusion can be reproduced, especially on the all-important issue of the surface heat fluxes. Second, we want to assure that the model will optimally simulate the warm pool behavior. Finally, we want to gain more insight into the role of the ocean fluxes in the annual cycle of the WHWP, and ultimately to diagnose the details of the WHWP heat budget that observations alone cannot resolve.

With those objectives in mind, the paper is organized as follows. In section 2, a description of the OGCM used is provided, followed by the details of numerical experiments and their

statistical scores in section 3. In section 4, we evaluate HYCOM forced with six surface wind and heat flux climatologies used in EL05, plus two newly available surface flux data sets, in the light of hydrographic data, to find the surface flux climatology that minimizes the model errors. In section 5, the fine-tuned model runs are then used to carry out a preliminary heat budget analysis of the WHWP. In section 6, forcing HYCOM with the most reliable flux climatology, HYCOM is further tested by using different parameterizations of light attenuation and turbulent vertical mixing. Finally, in section 7, a summary is given and the model’s skill in reproducing the observed WHWP cycle is evaluated.

2. Model configuration

a. HYCOM model

HYCOM is a primitive equation model developed from the Miami Isopycnal Coordinate Ocean Model (MICOM) [Bleck *et al.*, 1992]. The major improvement of HYCOM is in its treatment of the vertical coordinate [(Bleck, 2002)]. HYCOM mainly uses the potential density as the vertical coordinate as in MICOM, but it allows the vertical coordinate to become pressure-like (z-coordinate) near the ocean surface where diabatic processes are important, and uses sigma coordinates in shallow water depth regions. The major advantage of using such a complex vertical coordinate system is to provide appropriate vertical resolution in the surface mixed layer and shallow water depth area. The Krauss-Turner bulk mixed layer model, which is the only mixed layer model present in MICOM, may be adequate for mid-latitude oceans, but it cannot properly portray the vertical momentum shear within the mixed layer, which is particularly important in the equatorial oceans [Lee and Csanady, 1999]. The motivation for using HYCOM in this study is to achieve greater flexibility in mixing parameterizations as they impact the

shallow warm pool behavior. However, one trade-off is that HYCOM uses so-called the hybrid grid generator, which is a numerical scheme that reconstructs the layer structure during the model integration to match the predefined target density of each layer [Bleck, 2002]. The hybrid grid generator acts like an "upstream" vertical advection operator, which is known to be diffusive [Bleck, 2002]. The numerical diffusion of such nature can have serious consequences in the heat tendency of the non-isopycnal layers. Therefore, an anti-diffusion scheme is in place in the latest HYCOM release (version 2.1) to minimize the numerical diffusion. In this study, however, instead of applying the anti-diffusion scheme, we simply go around the problem by enforcing the non-isopycnal layers to have prefixed depths in the upper 50m throughout the model integration. In this way, the hybrid grid generator causes no numerical diffusion in our simulation, at least in the upper 50m. For more detailed description and recent development of HYCOM on the same issue and others, see Bleck [2002] and Halliwell [2004].

b. Model domain and configurations

As configured for this study, the model domain contains both the Pacific and Atlantic Oceans between 100°E and 20°E, bounded north and south by 65°N and 35°S. The grid resolution is uniform 1° zonally and variable in the meridional direction; 0.5° at the equator increasing linearly to 1° at 40° latitude and 1° poleward of 40°. It must be noted that, under such horizontal resolution, the mid-latitude western boundary currents and the associated hydrodynamic instabilities may not be properly resolved. Therefore, we have chosen a relatively large value of about 3000m²/s for the lateral heat, salt and momentum diffusivity. We use 5 fixed-depth layers (10m for each) for the upper 50m and 17 non-uniform hybrid layers for deeper ocean. The target densities for the 17 deeper layers are 23.25, 24.00, 24.70, 25.28, 25.77, 26.18, 26.52, 26.80,

27.03, 27.22, 27.38, 27.52, 27.64, 27.74, 27.82, 27.88, and 27.94 in σ_θ units, as optimized for the North Atlantic Ocean. The model is initialized with the January Levitus climatology [Levitus and Boyer, 1994; Levitus *et al.*, 1994], and fields at the five grid latitudes adjacent to the northern and southern boundaries are relaxed back to the monthly Levitus climatology with a damping time of approximately 3 months. The sea surface salinity (SSS) is updated by fully incorporating the precipitation data from whichever climatology is used. However, since the salinity is not the major focus in this study, the SSS (but not the SST) is relaxed back to the Levitus climatology with the e-folding time of 30 days. The grid structure in the eastern tropical Pacific and the tropical Atlantic, and the locations of the four subregions of the WHWP, are indicated in Figure 1. The geographic limits shown in this figure are referred to as the WHWP domain in the text. However, the full model domain used extends westward to 100°E so as to properly simulate the Pacific variability that impacts the ENP subregion. In all model experiments performed in this study, temperature and salinity are advected and diffused, and are also remapped by the hybrid grid generator, while the density is diagnosed from the equation of state.

c. Surface thermal forcing strategy

In the current version (version 2.1) of HYCOM, the wind stress vector, shortwave radiative heat flux and longwave radiative heat flux are specified inputs with no cross-interface interaction. The shortwave penetration below the ocean surface is computed by using the KPAR (attenuation coefficient for Photo-synthetically Available Radiation) climatology [Kara *et al.*, 2003] derived from SeaWiFS attenuation coefficient at 490nm [McLain *et al.*, 2002]. The turbulent surface fluxes are imposed interactively: the wind speed, air temperature and specific humidity, all measured at 10m above the sea surface, are specified and these along with the

model-produced SST are used to update the latent heat flux and sensible heat flux during the model integration. Simple bulk formulas are used to compute the surface turbulent heat fluxes [Liu *et al.*, 1979]:

$$Q_{EVP} = \rho L C_E |U| (q_a - q_s), \quad (1)$$

$$Q_{SEN} = \rho c_p C_S |U| (T_a - SST), \quad (2)$$

where ρ is air density ($1.2 \text{ kg}\cdot\text{m}^{-3}$), c_p is the specific heat of air at constant pressure ($1005.7 \text{ J}\cdot\text{kg}^{-1}\cdot\text{K}^{-1}$), L is the latent heat of evaporation ($2.47 \times 10^6 \text{ J}\cdot\text{kg}^{-1}$), C_E and C_S are the transfer coefficients for latent and sensible heat respectively, U is the wind speed at $z=10\text{m}$, q_a and T_a are specific humidity and temperature of air at $z=10\text{m}$, and q_s is the saturation specific humidity, which is computed in the model using the Clausius-Clapeyron equation represented by a sixth order polynomial in SST [Lowe, 1977]. For whichever heat flux climatology we apply to the model, we use the corresponding values of C_E and C_S . But, we use only the neutral values for the transfer coefficients because stability-dependent forms of the transfer coefficient, such as one used in the COARE3.0 algorithm [Fairall *et al.*, 2003; Kara *et al.*, 2004], are not useful when monthly averaged forcing data are used [Gulev, 1998]. For instance, when Southampton unconstrained heat flux climatology [SHU, Josey *et al.* 1998] is used, C_E and C_S are set equal to 0.0012 and 0.0010, respectively; when the Southampton constrained heat flux climatology [SHC, Grist and Josey, 2003] is used, the fractional adjustment factors, 1.19 and 1.07 are multiplied to the SHU values of C_E and C_S , respectively to be consistent with the global heat flux constraints as illustrated in Grist and Josey [2003]. See Zeng *et al.* [1998] and Renfrew *et al.* [2002] for more details about the bulk algorithms used in different heat flux products.

Alternatively, HYCOM can be forced directly with the actual net surface heat flux rather than recalculating the surface turbulent heat fluxes from bulk formula. In this case, however,

strong SST relaxation is usually required as in other ocean general circulation models (OGCMS). For example, *Gordon and Corry* [1991] and *Vialard et al.* [2001] used the damping rate of $35 \sim 40 \text{ W} \cdot \text{m}^{-2} \cdot \text{K}^{-1}$, which can be translated to approximately 1.5 days of *e*-folding damping time. Without a doubt, such a strong SST damping will reduce the SST error significantly. However, under such a forcing scheme, the SST damping term will be too strong, which make it very difficult to assess important SST forcing mechanisms.

3. Numerical experiments and statistical scores

Sixteen primary experiments are carried out (Table 1). In the first eight experiments, we explore the sensitivity of HYCOM to six of the surface wind and heat flux climatologies used in EL05, namely the da Silva unconstrained [DSU, *da Silva et al.* 1994], Oberhuber [OBH, *Oberhuber*, 1988], Southampton constrained [SHC, *Grist and Josey*, 2003], Southampton unconstrained [SHU, *Josey et al.*, 1998], NCEP/NCAR global reanalysis-1 [NCEP1, *Kalnay et al.* 1996] and the European Center for Medium Range Weather Forecasting (ECMWF) 15-year global reanalysis [ERA15, *Gibson et al.*, 1997]. Additionally, two newly available reanalysis products, NCEP/NCAR global reanalysis-2 [NCEP2, *Kanamitsu et al.*, 2002] and ECMWF 40-year global reanalysis [ERA40, *Brankovic and Molteni*, 2004] are also evaluated. The turbulent mixing model in those eight experiments is fixed with the non-local K-Profile Parameterization (KPP) model using the default parameter values [*Large et al.* 1994]. Note that the da Silva constrained heat flux [*da Silva et al.*, 1994] explored in EL05 is not used here because individual components of the surface heat flux terms, which are needed for HYCOM simulation, are not available.

Two additional experiments are carried out to explore the sensitivity of HYCOM to the parameterization of light attenuation; the solar attenuation depth is fixed to 23m in SHC-JW1-KPP and 17m in SHC-JW3-KPP. The SHC surface flux climatology is used in both experiments, having previously been found optimal. In the last six experiments, the sensitivity of HYCOM to different turbulent mixing parameterizations is explored by using the two turbulent mixing models, namely the non-local K-profile parameterization [KPP; *Large et al.*, 1994] and the NASA Goddard Institute for Space Studies level-2 turbulence closure [GISS; *Canuto et al.*, 2001, 2002]. The influences of the crucial parameters in the KPP model, the critical bulk Richardson number (Ric) and the critical gradient Richardson number (Ri_0) on the HYCOM simulations are examined (SHC-KPP-a; SHC-KPP-b; SHC-KPP-c; SHC-KPP-d). The importance of background diffusivity associated with internal wave breaking in the KPP model and its impact on the HYCOM simulations are also tested (SHC-KPP-e). Finally, the GISS turbulent mixing model is tested to compare with the KPP model. The SHC surface flux climatology is used in these last six experiments. All sixteen experiments reached an equilibrium state after about seven years, which was judged by the time evolution of basin-averaged kinetic energy. The model results used in the next sections are all based on the monthly average of model output for year 15.

The performances of the sixteen experiments are evaluated by comparing the model outputs of the warm pool SST with the corresponding values from the World Ocean Atlas 2001 (WOA01) climatology [*Conkright et al.*, 2002]. Table 2 shows the 95% confidence limits of the mean SST errors (simulated minus observed) obtained from the sixteen HYCOM experiments for the periods of peak warm pool development and for the areas of the four WHWP subregions. The last columns are totals for the entire warm pool and year. The values in the table are

prepared by first locating the WOA01 [Conkright *et al.*, 2002] grid points at which the observed SST is higher than 27.5°C, then interpolating the simulated SST to the WOA01 grid points to compute model-data differences. Using a bootstrap technique [Efron, 1979], the model SST errors at the WOA01 grid points for the given WHWP months and the WHWP sub-region are randomized to replicate 500 sets of extra realizations. Using those 500 sets of the mean SST error, the 95% confidence limit, which is approximately twice the standard deviation, is obtained. Note that the 95% confidence limit used here shows how well the mean SST error represents the model bias over the given WHWP months and WHWP sub-region.

Table 3 is the same as Table 2 except that the SST pattern correlation is provided instead of SST error. The pattern correlation is simply the spatial correlation between the simulated and observed SST for the given WHWP months and WHWP sub-region, and it does not provide any temporal correlation between the simulated and observed SST. The 95% confidence limits are obtained by using a bootstrap technique as explained above. In the following sections, the statistical test scores shown in Tables 2 and 3 are used to evaluate the model outputs from the sixteen experiments.

4. Sensitivity to surface wind and heat flux climatologies

a. Brief comparisons of the eight flux climatologies.

Before evaluating the model output, brief comparisons of the eight surface forcing climatologies are presented here. Figure 2a shows the eight annual cycles of the net heat flux averaged over the WHWP subregions, outlined in Figure 1. The convention in this paper is that the positive heat flux means heat gain for the ocean and the negative for heat loss. It can be seen that the net heat flux values of the four model-based reanalysis products (NCEP1, NCEP2,

ERA15 and ERA40) are in general substantially smaller (putting less heat into the ocean) than those of the Comprehensive Ocean-Atmosphere Data Set (COADS)-based climatologies. According to *Sun et al.* [2003], this is partly due to the systematic overestimation of latent heat flux in the reanalysis products. They found that the overestimation of the latent heat flux in the NCEP1, NCEP2 and ERA15 is about 29Wm^{-2} when it is averaged over the tropical Atlantic, and that it can be reduced significantly by recomputing the latent heat flux using the COARE2.6a bulk formula [*Fairall et al.*, 1996] applied to the reanalysis data of the specific humidity and wind speed. They compared the new estimations of the latent heat flux with the buoy observation in the PIRATA mooring locations, and found that the new estimations were much closer to the observations, suggesting that the bulk algorithms used in the reanalysis products are partly responsible for the overestimations of latent heat flux. Although the ERA40 was not assessed by *Sun et al.*, [2003], it appears that the ERA40 shares the same problem with other reanalysis products according to Figure 2a. In general, the net heat flux (into the ocean) is largest in the SHU and DSU, and smallest in the ERA15 data (in the ENP subregion, the net heat flux is smallest in NCEP2). It was also shown in EL05 that the SHU and DSU data yield unrealistically large residual values of total diffusive flux when compared with TOGA-COARE results, and that the NCEP1 and ERA15 data yield a non-physical diffusion of heat into the warm pools from their cooler surroundings. For the warm season, typical spreads between largest and smallest are about 100Wm^{-2} .

b. Bulk parameterization of surface turbulent heat flux

Figure 2b is same as Figure 2a except that the turbulent heat fluxes are recomputed using the bulk formulas as done in the HYCOM simulations (Eqs. 1 and 2); the World Ocean Atlas 2001

(WOA01) climatology [Conkright *et al.*, 2002] is used for SST, and the saturation specific humidity at the sea level pressure is computed from this SST product following Lowe [1977]. In the cases of DSU and OBH, the original (a) and the recomputed (b) net heat flux values are fairly consistent. But, the recomputed net heat flux values are substantially reduced in the cases of SHU and SHC, and increased in the four reanalysis products. This inconsistency between the two sets of net heat flux is attributable to the fact that the turbulent heat flux components in Figure 2b are computed from the monthly mean dataset of the air-sea interface variables (wind speed, specific humidity, air temperature and SST), which introduce a significant bias as discussed by Simmonds and Dix [1989] and Gulev [1997]. In order to avoid this problem, all the air-sea interface variables used in the bulk formulas must be measured at least every 6 hours. However, when climatological datasets such as the SHU and SHC are used, this heat flux bias is unavoidable. Gulev [1997] showed that the difference between the turbulent heat fluxes computed from time-mean atmospheric data (“classical” method) and that from synoptic interval data (“sampling” method) can be as large as $15 \sim 20 \text{ W} \cdot \text{m}^{-2}$ for sensible heat flux and $50 \sim 70 \text{ W} \cdot \text{m}^{-2}$ for the latent heat flux in the subtropical north Atlantic [see Zhang, 1995, 1997 for the discussion of the same issue over the equatorial Pacific Ocean]. He also showed that this bias originates from the non-zero correlations (largely at the diurnal time scale) among wind speed, transfer coefficients and air-sea temperature and humidity gradient, and demonstrated that the quantification of the global scale bias using the mean quantities is in general not possible because the biases are quite variable in time and space. For future reference, this bias is simply called anisotropic turbulent heat flux, hereafter.

To assess its impact, the anisotropic turbulent heat flux is estimated by recomputing the latent and sensible heat fluxes from bulk formulae using the monthly mean atmospheric

quantities (U , q_a , q_s and T_a) from the eight heat flux climatologies and SST from WOA01, then subtracting it from the original latent and sensible heat fluxes: this is the same as subtracting the right side values in the Figure 2 from the corresponding values in the left side. In the case of SHC data, for example, the recomputed latent heat flux is about $15.1\text{W}\cdot\text{m}^{-2}$ larger (more heat lost from the ocean) when averaged over all grid points in the WHWP domain and all twelve months, while the recomputed sensible heat flux is increased by $1.7\text{W}\cdot\text{m}^{-2}$ (more sensible heat flux from ocean to atmosphere). However, the anisotropic turbulent heat flux at individual grid points can vary from -80 to $80\text{W}\cdot\text{m}^{-2}$ in the ENP, and from -20 to $60\text{W}\cdot\text{m}^{-2}$ on the Atlantic side, such that there seems to be no systematic pattern in the temporal and spatial distributions. In order to minimize the turbulent heat flux bias introduced by non-zero anisotropic turbulent heat flux, a strategy taken here is to directly incorporate the twelve monthly values of the estimated anisotropic turbulent heat flux into HYCOM as an additional heat flux term. Note that our strategy used here is mainly based on observational evidence that the synoptic variability in the surface turbulent heat flux is independent of the long-term mean heat flux [Gulev, 1997]. This surface forcing strategy is used for all experiments in this study.

c. Simulated annual WHWP cycle

Figure 3 shows the observed warm pool SST from the World Ocean Atlas 2001 (WOA01) climatology [Conkright *et al.*, 2002] versus the simulated warm pool SST from the eight experiments (SHC-KPP, OBH-KPP, SHU-KPP, DSU-KPP, NCEP1-KPP, NCERP2-KPP, ERA15-KPP and ERA40-KPP) in February, April, June, August and October. In the cases of SHC-KPP and OBH-KPP, there is a good visual correlation between the simulated and observed SST maps. In those two experiments, the model successfully simulates the size and shape of the

ENP and EQA warm pools in spring, as well as the GoM and CBN warm pools in boreal summer. It is also seen that the early spring SST structure over the ENP due to the Tehuantepec and Papagayo mountain pass wind jets [McCreary *et al.*, 1989; Chelton *et al.*, 2000] is well simulated in both cases. However, the simulated SST in the SHC-KPP and OBH-KPP also shows some problems as well. In particular, both the SHC-KPP and the OBH-KPP simulations yield higher SST over the warmest portions of the warm pool off the Gulfs of Guinea (in EQA), Tehuantepec and Papagayo (in ENP), with the OBH-KPP bias being the greater of the two. Another problem observed in both experiments is that the central equatorial Atlantic, where a cold-water tongue appears in boreal summer, is too cold in April.

Table 2 shows that the mean SST bias in the OBH-KPP experiment remains fairly small (± 0.25). The mean SST bias in the SHC-KPP experiment ranges between -0.41°C (EQA) and 0.18°C (ENP), and remains small in the GoM and CBN ($-0.09 \sim 0.00^{\circ}\text{C}$). The SST pattern correlation is generally higher in the SHC-KPP than in the OBH-KPP, but it is particularly low over the EQA in both experiments as shown in Table 3. When averaged for all four WHWP sub-regions, the SST bias is not significantly different in the two experiments, but the pattern correlation is significantly higher in SHC-KPP than in OBH-KPP.

When HYCOM is forced with the two unconstrained climatologies, namely SHU and DSU, the simulated WHWP is too warm and its area too large, but more so for the latter. The SST bias is as large as 1.52°C in those cases (Table 2). Despite the large bias in the WHWP SST, the SST pattern correlations of the two experiments are not significantly lower than those of the SHC-KPP and OBH-KPP experiments. In those two cases, the model does not suffer from the negative SST bias over the central equatorial Atlantic as in the SHC-KPP and OBH-KPP.

The simulated SST in the NCEP1-KPP and NCEP2-KPP experiments are in better agreement (cooler, smaller) with the observations than SST in the two unconstrained forcing experiments (SHU-KPP and DSU-KPP). The simulated warm pool SST is in general higher and the area larger in the NCEP1-KPP than in the NCEP2-KPP experiment, with this difference being most striking in the ENP and EQA. In both ERA15-KPP and ERA40-KPP experiments, the Atlantic side of the simulated WHWP is colder and its area smaller than observed, while the ENP warm pool is warmer and its area larger than observed in the ERA40-KPP experiment. In the case of ERA15-KPP, in particular, the CBN warm pool nearly disappears in the boreal summer months. The mean SST bias in the ENP is relatively small in the NCEP2-KPP and ERA15-KPP experiments (Table 2), but the mean SST in the EQA warm pool is negatively biased by up to -1.22°C in the NCEP2-KPP experiment, and the mean SST in the GoM, CBN and EQA are all negatively biased by $-1.63 \sim -1.26^{\circ}\text{C}$ in the ERA15-KPP experiment. The SST pattern correlation values in the NCEP1-KPP, NCEP2-KPP, ERA15-KPP, and ERA40-KPP experiments are significantly lower than the corresponding values in the SHC-KPP experiment (Table 3).

The net surface heat flux into the WHWP is much larger in the DSU data than in the ERA15 data, by more than 100W/m^2 , suggesting that the surface heat flux bias is the most likely source of the model SST bias. Figure 4 shows the linear regression of the model SST bias and the net surface heat flux from grouped for each WHWP sub-region. A close inspection of the figure suggests that the warm (cold) mean SST biases in the eight HYCOM experiments are indeed largely explained by the higher (lower) net heat flux values onto the corresponding WHWP sub-regions. We found no such clear correlation between the model SST bias and the wind stress curl (zonal wind stress for the EQA) from the eight experiments.

Figure 5 shows the annual cycle of the simulated versus observed (WOA01) subsurface temperature profile over the four WHWP subregions. For better comparison, thicker lines are used for 20, 24 and 28°C. The values used in the plot are obtained by averaging the temperature over the $10^\circ \times 5^\circ$ box near the center of each WHWP subregion (see Figure 1). In agreement with the WOA01, the thermocline layer in all eight experiments is well developed in the EQA and ENP, and it is much shallower than those in other warm pool subregions, although the shallow thermocline is weaker than the data show. The thermocline layer in the ENP deepens in spring months until May, which is the peak month of the ENP warm pool. The deepening of the thermocline in the ENP during boreal spring is consistent with the reduction of the positive wind stress curl during the same period (not shown). The shoaling of the thermocline in EQA during boreal summer is associated with the basin-wide strengthening of the easterlies along the equator (not shown). Unlike the EQA and ENP, the simulated stratification below the mixed layer is both weaker and deeper in the GoM and CBN. The main features in the annual cycle of the subsurface temperature profile just described are well captured in all eight experiments. However, in all experiments, the modeled subsurface water column is warmer and its stratification weaker than observed. Since such model bias in the thermocline occurs in all experiments regardless of the surface heat flux data used, it is apparent that the model is biased. This issue regarding the weaker-than-observed stratification in the modeled thermocline is investigated further in section 6.

In summary, we find that the annual evolution of WHWP is best simulated in the SHC-KPP and OBH-KPP experiments, with the mean SST bias ranging between -0.41°C (EQA) and 0.18°C (ENP) in the case of SHC-KPP experiment. When HYCOM is forced with the two unconstrained heat flux climatologies, SHU and DSU, the simulated WHWP is too warm and its area too large,

indicating that the two unconstrained heat flux climatologies put too much heat into the WHWP as concluded in EL05. When HYCOM is forced with the model-based reanalysis heat flux products, the Atlantic side of the simulated WHWP is usually colder and its area smaller than observed, with the ERA15-KPP being the extreme of all four. Nevertheless, the mean SST bias in the ENP warm pool is quite small in the NCEP2-KPP and ERA15-KPP experiments, while a positive mean SST bias occurs in the NCEP1-KPP and ERA40-KPP experiments. In the case of NCEP1-KPP experiment, the mean SST bias is positive in the ENP and EQA, and negative in the GoM and CBN. These results regarding the NCEP1-KPP and ERA15-KPP experiments are consistent with EL05 where it was shown that the ERA15 data put too little heat into the four WHWP subregions, while the NCEP1 data put too little heat in the GoM and CBN warm pools.

Based on the model SST bias and statistical scores in the eight experiments, here we conclude that the SHC and OBH surface heat flux data are the most reliable heat flux climatologies for reproducing the observed annual WHWP cycle, consistent with EL05. In the next section, the WHWP heat budget obtained from the eight experiments is discussed to describe the annual heat budget of the WHWP.

5. Preliminary heat budget analysis of WHWP

The integral of the heat conservation equation over the warm pool slab bounded by the sea surface and the fixed side and bottom boundaries yields,

$$\underbrace{\frac{d}{dt} \iiint \rho c_p T dv}_{Q_{STR}} = \underbrace{\iint R|_{z=0} dA + \iint \left. \frac{\partial \overline{w' T'}}{\partial z} \right|_{z=0} dA}_{Q_{NET}} + \underbrace{\iint R|_{z=d} dA}_{Q_{SWP}} + \underbrace{\iint \rho c_p T \mathbf{v} \cdot \mathbf{n} dA}_{Q_{ADV}} + \underbrace{\iint \left. \frac{\partial \overline{w' T'}}{\partial z} \right|_{z=d} dA}_{Q_{DIF}}, \quad (3)$$

where ρ is the water density, c_p is the specific heat of sea water, R is the radiative heat flux at a given depth and d is the slab depth. The LHS is the heat storage rate (Q_{STR}), the RHS are the

surface net heat flux (Q_{NET}), the shortwave penetration at the slab base (Q_{SWP}), the advective heat flux divergence (Q_{ADV}) and the diffusive heat flux across the slab base (Q_{DIF}), respectively. Note that the horizontal sub-grid diffusion term, although it is a part of the model heat equation, is not included in (3) because it is usually very small. As noted earlier, the heat flux terms are obtained by first computing them at each time step during the model integration of the year 15, then taking the monthly average, thus the advective heat flux divergence term (Q_{ADV}) contains both mean and eddy contributions.

Figure 6 shows the observed (thick solid line) versus simulated seasonal cycle of the volume-averaged temperature (first panel) and slab heat budget terms (Q_{STR} , $Q_{NET} + Q_{SWP}$ and $Q_{ADV} + Q_{DIF}$) of the ENP obtained from the WOA01 and the eight experiments, respectively. The depth of the slab is taken as 20m, which is the approximate depth of 27.5°C for the ENP (EL05). As shown in the first panel, the ENP slab temperature is overestimated in all eight experiments by up to 1.86°C (DSU-KPP). The model bias in slab temperature is larger than the SST bias (Table 2), due mainly to the model's failure in reproducing the sharp thermocline near the ENP slab base (see Figure 5)). The simulated heat storage rate (Q_{STR}) has larger than observed seasonal variation, up to 13.7W/m² (DSU-KPP) during boreal spring and summer.

The SHU-KPP and DSU-KPP are disqualified due to their large biases in ENP slab temperature. In the case of NCEP1-KPP, the ENP warm pool continues to exist till mid-November disagreeing with the observation. This suggests that the NCEP1 data overestimates the surface net heat flux into the ENP in boreal summer. Both the slab temperature and heat storage rate are least biased in the SHC-KPP. According to the SHC-KPP experiment, during the onset phase of the ENP slab (FMA), the surface net heat flux ($Q_{NET} + Q_{SWP} = 50.4\text{W/m}^2$) forces the warming of the ENP slab while the diffusive heat flux (-14.2W/m^2) and advective flux

divergence (-11.9W/m^2) damp out the heat. The decay phase (JJA) starts after the peak in May and the rapid reduction of the surface net heat flux ($Q_{NET} + Q_{SWP} = 5.3\text{W/m}^2$) helps the ENP to cool off. The diffusive (-6.5W/m^2) and advective cooling (-9.2W/m^2) is slightly less intense in the decay phase (JJA).

Figure 7 is the same as Figure 6 except for the GoM slab. The depth of the GoM slab is chosen to 20m following EL05. The GoM slab temperature is overestimated in the SHU-KPP and DSU-KPP for all months, and underestimated in ERA15-KPP for summer and fall months. However, the seasonal cycle of the heat budget terms are in good agreement in all eight experiments. The GoM slab undergoes warming during March to July and cooling in other months. During the winter months, the GoM experiences an intense cooling at the surface, thus a convective adjustment takes place mixing the colder surface water with the warmer water below. The convective warming of the cold surface water is responsible for the positive diffusive heat flux during the winter months. As in the case of the ENP slab, the surface net heat flux is the major forcing terms in the GoM slab. The advective heat flux divergence is relatively insignificant ($-10.4 \sim 16.9\text{W/m}^2$).

The CBN slab temperature is overestimated in the SHU-KPP and DSU-KPP (Figure 8), while it is underestimated in the OBH-KPP, NCEP1-KPP, ERA15-KPP and ERA40-KPP. It is well simulated in the SHC-KPP and NCEP2-KPP. In the case of NCEP2-KPP, however, the heat storage rate turns negative too early in September disagreeing with the observations. According to the SHC-KPP, the warming of the CBN slab starts from early March as in the GoM slab, but continues further to the mid-September. The heat storage rate is much larger in the earlier stage of the warming (April and May) and weaker afterward (JJAS). The advective heat flux divergence is insignificant between March and April, but it becomes the major cooling source

between June and September (-19.9W/m^2), contributing to the significant reduction in the heat storage rate in onset and peak phases. The net effect is the mild increase of the slab temperature between June and September as shown in the first panel. During the decay phase (OND), the advective heat flux divergence becomes less important (-6.9W/m^2). The diffusive cooling rate is relatively small throughout the entire warming months between March and September ($-9.0 \sim -4.9\text{W/m}^2$). As in the ENP and GoM slabs, the monthly variation of the surface net heat flux is the major forcing term for the CBN slab cycle.

As in other warm pool slabs, both the slab temperature and heat storage rate for the EQA are least biased in the SHC-KPP. However, the model's performance in the EQA slab is quite poor (Figure 9) in other experiments. In particular, the annual cycle of heat storage rate in the NCEP2-KPP and ERA15-KPP is extremely unrealistic, suggesting that the two surface heat flux data sets, NCEP2 and ERA15 are not reliable over the EQA subregion (see Figure 2). According to the SHC-KPP, the EQA slab, located near the Gulf of Guinea and the eastern equatorial Atlantic, is very different from other WHWP regions, since the onset and decay of the EQA slab is largely controlled by the annual cycle of the advective heat flux divergence. The diffusive heat flux is also quite large throughout year ranging between -10.8W/m^2 in February and -29.4W/m^2 in June. The overall impact of the surface net heat flux is much less than the advective heat flux divergence term. The advective cooling intensified during the decay phase is mainly associated with equatorial upwelling, which results in the appearance of cold-water tongue in boreal summer. Therefore, the horizontal component of the advective heat flux divergence is less significant compared to the vertical component, ranging between -15.0 (June) and 4.9W/m^2 (February), although the eddy mixing must be an important warming mechanism locally over the cold-water tongue region [Foltz *et al.*, 2003; Vialard *et al.*, 2001; Weingartner and Weisberg,

1991]. The vertical component of the advective heat flux divergence ranges from -55.0 (May) to -9.4W/m² (October).

6. Additional sensitivity experiments

In the previous sections, it is shown that the SHC serves as the best surface heat flux climatology for the simulating the annual cycle of WHWP. However, the simulated thermocline is warmer and its stratification weaker than observed, regardless of the surface heat flux data used, indicating that the model is biased. Therefore, we now explore further the sensitivity of the simulated WHWP to different choices of light attenuation and turbulent diffusion models.

a. Sensitivity to the parameterization of light attenuation

Following the pioneering work of *Jerlov* [1976], open oceans are usually categorized to Jerlov water type-1 (subsequently refined to type 1-A or 1-B), which corresponds to an attenuation depth of 23m or so. This value has been widely used in ocean modeling and mixed layer heat budget studies [e.g., *McPhaden*, 1982; *Wang and McPhaden*, 1999; *Faltz et al.*, 2003]. *Rochford et al.* [2001], calibrating the SeaWiF data against the spectral attenuation coefficient at 490nm (K490), constructed a climatology of KPAR, which represents the effective attenuation coefficient for the broader 350-700nm ranges, which is more representative of the overall shortwave spectrum penetrated into the ocean than is the single frequency of 490nm. Accordingly, the KPAR light penetration depth in optically clear water is less than indicated by Jerlov type I or by K490, barely exceeding 17m. Decreasing the attenuation depth may affect ocean model behavior in two ways. An obvious impact is the increase in the vertical gradient of penetrative shortwave heat flux below the sea surface. As a result, the static stability in the

surface water column increases, thus reducing the vertical turbulent mixing and increasing the surface layer temperature. Therefore, the net effect of decreasing attenuation depth is an increase in SST and a shoaling of the mixed layer, and vice versa for increasing attenuation depth. In order to explore the sensitivity of HYCOM to the parameterization of light attenuation, two model experiments are carried out using light attenuation depths that represent the optically clear water in KPAR, 17m (SHC-JW3-KPP) and in the K490, 23m (SHC-JW1-KPP).

As indicated in Table 2, decreasing the attenuation depth from 23m (SHC-JW1-KPP) to 17m (SHC-JW3-KPP) increases the simulated SST quite substantially in all four WHWP subregions (up to $\sim 0.2^{\circ}\text{C}$ in ENP), probably due to the mechanism just described. The conventional value of $\sim 23\text{m}$ for the light attenuation depth (Jerlov water type-1) produces a large negative SST bias, which is much reduced when the constant attenuation depth of 17m is used instead. As shown by *Kara et al.* [2004], we also find that the SST predicted with variable KPAR climatology (SHC-KPP) is much closer with the observation, suggesting that the spatially varying attenuation depth has non-negligible impact on upper tropical oceans [*Murtugudde et al.*, 2002]. For accurate simulation of the WHWP SST, therefore, it is necessary to use the light attenuation depth profiles from the monthly KPAR climatology. The simulated thermocline is, however, still warmer and its stratification weaker than observed in the two experiments (SHC-JW1-KPP and SHC-JW3-KPP), and it is not affected much by different choice of light attenuation depth model (not shown).

b. Sensitivity to turbulent mixing parameterizations

Halliwell (2004) evaluated several vertical-mixing schemes available for use in HYCOM. In his study, it was clearly shown that the KPP model outperforms other mixing schemes.

Therefore, we have selected the KPP mixing algorithm as the default turbulent mixing scheme in the HYCOM experiments. Although the KPP model is well documented by *Large et al.* [1994] and its implementation in HYCOM by *Halliwel* [2004], here we briefly describe how the vertical heat diffusion is determined in the KPP model. The vertical turbulent diffusion of heat is parameterized in the KPP model by

$$\overline{w'\theta'} = -h_b l G \left(\frac{\partial \bar{\theta}}{\partial z} + \gamma \right), \quad (4)$$

where G is a predefined smooth function (a third order polynomial) in z , l is the turbulent length scale, γ is the non-local transport term (which is zero as long as the net surface heat flux is stabilizing (*i.e.*, $Q_{NET} > 0$) therefore usually unimportant in the WHWP), and h_b is the surface boundary layer thickness. The turbulent length scale (l) is determined from the frictional velocity and the convective velocity scale, which are computed from local shear stress and surface heat flux, respectively. The surface boundary layer thickness (h_b), which is distinct from the mixed layer depth, is estimated by locating the depth at which the bulk Richardson number (Ri) attains its critical value, Ric - the surface boundary layer is usually shallower than the mixed layer depth. The heat diffusion below the surface boundary layer is obtained based on an equation similar to (4), but it is determined as a sum of three contributions, namely shear instability, internal wave breaking and double diffusion. The interior diffusivity associated with shear instability is a function of gradient Richardson number Ri_g , and for small Ri_g , it can be as large as $5 \times 10^{-3} \text{ m}^2/\text{s}$. On the other hand, the internal diffusivity associated with internal wave breaking is much smaller and usually assumed constant, $1 \times 10^{-5} \text{ m}^2/\text{s}$. Although small, this term is important where the gradient Richardson number, Ri_g is larger than its critical value Ri_0 (due to weaker vertical shear or stronger stratification). Note that Ri_0 is an adjustable parameter in the KPP

model, and it is different from the bulk critical Richardson number Ric ; *Large et al.* [1994] suggested $Ri_0 = 0.7$. The impact of the double diffusion in ocean general circulation model (OGCM) is pretty much unknown, but *Zhang et al.* [1998] showed that the strength of the meridional overturning circulation in the Atlantic Ocean simulated by a Geophysical Fluid Dynamics Laboratory (GFDL) model is quite sensitive to the parameterization of this term. In this study, the vertical diffusion due to double diffusion is kept in the KPP model, but the sensitivity of HYCOM to this parameterization is not examined.

As in other shear-driven mixing models, the critical bulk Richardson number Ric is the most important parameter in the KPP model. *Large et al.* [1994] suggested $Ric = 0.3$, which is slightly greater than the theoretical value of 0.25 found by *Howard* [1961]. The original definition of the critical Richardson number is that a small perturbation does not grow in time if the local Richardson number is everywhere greater than or equal to Ric [*Howard*, 1961]. Therefore, the turbulent motion is not necessarily subdued for $Ri > 0.25$ [*Canuto et al.*, 2001]. According to an observational study by *Martin* [1985], the finite amplitude turbulence ceases to exist when $Ri \sim 1$, although a sharp decrease in the diffusivity at $Ri = 0.25$ was observed in a large-eddy simulation [*Wang et al.*, 1996]. While the KPP model is formulated based on empirical equations, the GISS model and the Mellor and Yamada's level-2.5 turbulence closure model [MY2.5; *Mellor and Yamada*, 1982] are, on the other hand, formulated based on turbulent eddy energy equations. Higher order terms are parameterized based on laboratory experiments such as turbulence measurements in wind tunnels. The critical bulk Richardson number, Ric is specified implicitly as ~ 0.2 in the MY2.5 model and as ~ 1.0 in the GISS model, but in the KPP model it is an adjustable parameter. If Ric is increased in the KPP model, it is expected that the turbulent

mixing be enhanced in the WHWP, thereby increasing the surface boundary layer thickness and reducing the SST, and vice versa.

In order to explore the model's sensitivity to the two Richardson numbers, Ric and Ri_0 , four experiments are performed: SHC-KPP-a ($Ric=1.00$; $Ri_0=1.00$); SHC-KPP-b ($Ric=1.00$; $Ri_0=0.25$); SHC-KPP-c ($Ric=0.25$; $Ri_0=1.00$); SHC-KPP-d ($Ri=0.25$; $Ri_0=0.25$). Note that the default values for Ric and Ri_0 used in the previous experiments are 0.3 and 0.7, respectively. Additionally, another experiment is carried out, again using the KPP model but setting the heat diffusivity associated with the internal wave breaking to zero (SHC-KPP-e). Other KPP model parameter values used in this study are identical to the original values used in Large et al. (1994). Finally, the GISS model is tested (SHC-GISS) and its result is compared with the KPP model experiments.

As indicated in Table 2, it is quite clear that using different values for Ric or Ri_0 in the KPP model has no dramatic effect on the simulation of the WHWP since the mean SST bias and SST pattern correlation are surprisingly close in the four experiments, SHC-KPP-a ~ SHC-KPP-d. In fact, it is quite difficult to judge whether one experiment is more realistic than other three. However, this does not mean that the vertical shear is not important in the WHWP regions. On the contrary, the correlation between the diffusive heat flux and the vertical shear at the warm slab pool base is quite strong (not shown), suggesting that the shear driven mixing is an important process and reasonably well represented in HYCOM. A rather serious impact occurs when the heat diffusion associated with internal-wave breaking is removed from the KPP model (SHC-KPP-e). In this case, the mean SST bias increases by $0.05 \sim 0.11^\circ\text{C}$ (Table 2). The GISS model performs as well as the KPP model in all respects (see Table 2 and 3). The magnitude and sign of mean SST bias in the SHC-GISS experiment are quite close to those in the SHC-KPP

experiment, in which both Ric is set equal to 0.30. Considering that Ric is implicitly set to 1.00 in the GISS model, this again suggests that the choice of critical Richardson number is not critical in simulating the annual cycle of the WHWP, as long as it is in the range of 0.25 ~ 1.00.

The annual cycle of the subsurface temperature profiles in the four WHWP subregions obtained from the SHC-KPP-a, SHC-KPP-d and SHC-KPP-e experiments shows that a different choice of the critical Richardson numbers does not have a profound impact in the thermocline below the warm pool (not shown). There, the impact of removing the background diffusivity associated with internal-wave breaking is more noticeable. The thermocline layers in the EQA and ENP warm pools are slightly thinner in the SHC-KPP-e experiment in comparison with the SHC-KPP-a ~ SHC-KPP-d (not shown). This indicates that the background diffusivity is a more important parameter than the critical Richardson numbers for fine-tuning the KPP model in simulating the WHWP.

7. Summary and Discussions

In order to simulate properly the annual cycle of the WHWP, HYCOM is fine-tuned by exploring its sensitivity to eight widely used surface flux products, then to the parameterizations of light attenuation and turbulence mixing. The outputs from a total of sixteen model experiments are analyzed in comparison with observations, to finally arrive at the following major conclusions.

When monthly averaged surface heat flux climatology is used to force HYCOM, the surface turbulent heat fluxes (*i.e.*, latent and sensible heat fluxes) need to be adjusted to compensate for biases arising from nonlinearities at the unresolved shorter time scales. Without this parameterization, a significant difference of the surface turbulent heat flux occurs between the

original heat flux data and the actual heat flux used in HYCOM. This heat flux bias originates from non-zero anisotropic turbulent heat flux. In order to minimize its negative impact on the model simulation, a strategy taken here is to incorporate directly the anisotropic turbulent heat flux into the model as a separate heat flux term.

The magnitude of surface net heat flux into the WHWP varies by as much as $100\text{W}\cdot\text{m}^2$ among the eight heat flux climatologies used here. HYCOM is therefore very sensitive to which heat flux climatology is used. Among the eight surface heat flux climatologies assessed in this study, we find that HYCOM is most compatible with the SHC and OBH heat flux data; in particular, when the SHC data is used, the simulated SST and the warm pool depth is closest to observations. The SHU and DSU, which are unconstrained heat flux climatologies, put too much heat into the model WHWP thus creating unrealistically warm surface water, while the four model-based reanalysis heat flux products (NCEP1, NCEP2, ERA15 and ERA40) typically put too little heat into the WHWP, thus creating unrealistically cold surface water. This result is consistent with the conclusions of EL05, which are based solely on data.

A preliminary WHWP heat budget analysis is carried out using mainly the output of the SHC-KPP experiment. The forcing mechanisms for the onset and decay are quite different among the four WHWP regions. The major forcing mechanism is surface net heat flux for the ENP, GoM and CBN, while advective heat flux divergence serves as the major forcing mechanism in the EQA. Apart from the EQA, the advective heat flux divergence is not the major forcing term, but its contribution in the annual heat budget is quite significant in the ENP and CBN. Over the ENP, the advective heat flux divergence is a persistent yearlong cooling mechanism, while in the CBN increased advective heat flux divergence during the onset and

peak phases slows down the warming of the CBN considerably. We found no evidence that the advective heat flux divergence is important in the GoM.

Additional sensitivity experiments suggest that, in general, the simulated WHWP is much less sensitive to our tunings of light attenuation and turbulent mixing models. However, the model's performance is optimal in reproducing the WHWP SST if the light attenuation depth is derived from the monthly KPAR climatology; using the conventional value for the light attenuation depth of ~23m produces a negative SST bias in the WHWP regions. Additionally, the simulated WHWP SST does not appear to be very sensitive to the choice of critical Richardson number as long as it is within the range of 0.25 ~ 1.00. When the KPP mixing model is used, the background diffusivity due to internal wave breaking, although small, has more significant impact on the model WHWP SST. Removing this term in the KPP model results in an increase in mean SST bias by up to 0.11°C in the ENP warm pool.

The modeled thermocline water is warmer and its stratification weaker than observed in all sixteen experiments. Since such bias in subsurface temperature exists regardless of the surface heat flux data, the light attenuation model or the turbulent mixing parameterization used, it is suspected that the problem originates from other shortcomings in HYCOM. In particular, we expect that increasing the vertical grid resolution over the thermocline layer reduce the model bias in subsurface stratification, although numerical diffusion due to the hybrid grid generator may still be a problem. Another related factor is misrepresentation of the non-linear response of the surface mixed layer to high frequency forcing (synoptic and diurnal) in the current model. Finally, the current model has the zonal grid resolution of ~100km on the equator, which barely resolves the tropical instability waves [TIWs, 600 ~ 1200km in wavelength; *Legeckis and Reverdin*, 1987], which are the largest transient features in the WHWP domain, and considered

to be one of the important contributors in the heat budget of the equatorial Atlantic ocean (Foltz et al., 2003; Vialard et al., 2001; Weingartner and Weisberg, 1991). Other transient features, such as the North Brazil Current rings, are smaller yet. Therefore, in this study we have decided to use a relatively large value of the horizontal eddy heat diffusion coefficient to mimic the mixing due to current-eddy interaction. *Weingartner and Weisberg* [1991] obtained the horizontal eddy diffusion coefficient of approximately $2000\text{m}^2/\text{s}$ at the equator near 28°W when the TIWs are active in boreal summer. We have used a value slightly larger ($3000\text{ m}^2/\text{s}$) in all the HYCOM experiments in order to suppress the additional numerical noise. The horizontal momentum dissipation coefficient is also set to $3000\text{ m}^2/\text{s}$ in all the experiments. Because we have used a relatively large value of the momentum dissipation coefficient, hydrodynamic instability is suppressed in the model simulations. Therefore, the role of oceanic eddies in the WHWP dynamics are to be pursued in a future high-resolution model study. However, it is quite possible that the inability of the current model to resolve the TIWs is the major cause for the negative SST bias in the central equatorial Atlantic observed in the SHC-KPP, since their role is to transfer heat into the equatorial strip from the off-equatorial region.

We select the eight experiments, SHC-KPP, SHC-JW3-KPP, SHC-KPP-a, SHC-KPP-b, SHC-KPP-c, SHC-KPP-d, SHC-KPP-e and SHC-GISS satisfactory for simulating the annual cycle of the WHWP (see Table 1). In the case of SHC-KPP experiment, for example, the mean SST bias ranges between -0.41 (EQA) and 0.18°C (ENP). The model SST bias is minimized by using the SHC flux climatology and also by incorporating the anisotropic turbulent heat flux directly into the model as an additional heat flux term. Our conclusion regarding the model's sensitivity to the parameterizations of light attenuation and turbulent mixing are based on the notion that the heat flux bias in the SHC data is negligible. However, in principle, unless the

surface heat flux data are absolutely error-free, exploring the model's sensitivity to different model parameterizations or fine-tuning the model adds nothing in terms of understanding the source of model bias and how to minimize it. Certainly, the SHC climatology is not error-free, although in agreement with EL05 it seems to be the best of available choices. Therefore, there are certain limitations in interpreting the model errors in the seven experiments. More specifically, we cannot select one model parameterization over others solely based on the statistical scores, since the magnitude of the surface heat flux bias is unknown and presumably not negligible. Therefore, we select all the eight experiments as the fine-tuned experiments. However, the model errors obtained for each eight experiment must be fully accounted for in future modeling studies of the WHWP.

Acknowledgements. Our thanks to George Halliwell, Jr., Birol Kara, Alan Wallcraft and Joe Metzger for many useful conversations and exchanges about HYCOM and to Alberto Mestas-Nunez, Birol Kara, George Halliwell, Jr. and Rick Lumpkin for their pre-submission reviews of the manuscript. We also thank two anonymous reviewers for their useful suggestions, which led to a significant improvement of the paper. This research was supported by the NOAA PACS/GAPP Program through awards under Cooperative Agreement NA67RJO149 to the Cooperative Institute for Marine and Atmospheric Studies.

References

- Alexander, M. and J. Scott, 2002: The influence of ENSO on air-sea interaction in the Atlantic. *Geophys. Res. Lett.*, 29, 10.1029/2001GL014347.
- Bleck, R., C. Rooth, D. Hu, and L. T. Smith, 1992: Salinity-driven thermocline transports in a wind- and thermohaline-forced isopycnic coordinate model of the North Atlantic. *J. Phys. Oceanogr.*, 22, 1486-1505.

- Bleck, R., 2002. An oceanic general circulation model framed in hybrid isopycnic-Cartesian coordinates. *Ocean Model.*, 4, 55–88.
- Bosilovich, M. G., 2002: On the vertical distribution of local and remote sources of water for precipitation. *Meteorol. Atmos. Phys.*, 80, 31–41.
- Brankovic, C. and F. Molteni, 2004: Seasonal climate and variability of the ECMWF ERA-40 model. *Climate Dyn.*, 22, 139–155.
- Canuto, V. M., A. Howard, Y. Cheng, and M. S. Dubovikov, 2001: Ocean turbulence. Part I: one-point closure model. Momentum and heat vertical diffusivities. *J. Phys. Oceanogr.*, 31, 1413–1426.
- Canuto, V. M., A. Howard, Y. Cheng, and M. S. Dubovikov, 2002: Ocean turbulence. Part II: vertical diffusivities of momentum, heat, salt, mass, and passive scalars. *J. Phys. Oceanogr.*, 32, 240–264.
- Chelton, D. B., M. H. Freilich, and S. K. Esbensen, 2000: Satellite observations of the wind jets off the Pacific coast of central America. Part II: Regional relationships and dynamical considerations. *Mon. Wea. Rev.*, 128, 2019–2043.
- Conkright, M. E., T. D. O'Brien, T. P. Boyer, C. Stephens, R. A. Locarnini, H. E. Garcia, P. P. Murphy, D. Johnson, O. Baranova, J. I. Antonov, R. Tatusko, R. Gelfeld, and I. Smolyar, 2002: World Ocean Database 2001, CD-ROM Data Set Documentation. Silver Spring, MD, National Oceanographic Data Center, 137 pp.
- Charnock, H. 1955: Wind stress on a water surface. *Quart. J. Roy. Meteorol. Soc.*, 81, 639–640.
- da Silva, A. M., C. C. Young, and S. Levitus, 1994: Atlas of surface marine data 1994. Vol. 1, Algorithms and procedures. NOAA Atlas NESDIS 6, US Dept. of Commerce, 83 pp.
- Efron, B. 1979: Computers and the theory of statistics: thinking the unthinkable. *SIAM Rev.*, 21, 460–480.
- Enfield, D. B., and D. A. Mayer, 1997. Tropical Atlantic sea surface temperature variability and its relation to El Niño-Southern Oscillation. *J. Geophys. Res.*, 102, 929–945.
- Enfield, D. B., and S.-K. Lee, 2004: The heat balance of the Western Hemisphere Warm Pool. *J. Climate*, In press.
- Fairall, C. W., D. P. Rogers, J. B. Edson, and G. S. Young, 1996: Bulk parameterization of air-sea fluxes for Tropical Ocean-Global Atmosphere Coupled-Ocean Atmosphere Response Experiment. *J. Geophys. Res.*, 101, 3747–3764.
- Fairall, C. W., E. F. Bradley, J. E. Hare, A. A. Grachev, and J. B. Edson, 2003: Bulk parameterization of air-sea fluxes: Updates and verification for the COARE algorithm. *J. Climate*, 16, 571–591.
- Foltz, G. R., S. T. Grodsky, and J. A. Carton, 2003: Seasonal mixed layer heat budget of the tropical Atlantic Ocean. *J. Geophys. Res.*, 108, 3146, doi:10.1029/2002JC001584.
- Gibson, J. K., P. Kållberg, S. Uppala, A. Hernandez, A. Nomura, and E. Serrano, 1997: ERA description. *Re-Analysis (ERA) Project Report Series No. 1*, 72 pp.
- Gordon, C. and R. A. Corry, 1991: A model simulation of the seasonal cycle in the tropical Pacific Ocean using climatological and modeled surface forcing. *J. Geophys. Res.*, 96, 847–864.
- Grist, J. P. and S. A. Josey, 2003: Inverse analysis adjustment of the SOC air-sea flux climatology using ocean heat transport constraints. *J. Climate*, 16, 3274–3295.
- Gulev, S. K., 1997: Climatologically significant effects of space-time averaging in the North Atlantic sea-air heat flux fields. *J. Climate*, 10, 2743–2763.

- Halliwel, G. R., 2004: Evaluation of vertical coordinate and vertical mixing algorithms in the HYbrid-Coordinate Ocean Model (HYCOM). *Ocean Model.*, 7, 285-322.
- Howard, L. N., 1961: Note on a paper by J. W. Miles. *J. Fluid Mech.*, 10, 509-512.
- Jerlov, N. G., 1976: Marine Optics. Elsevier Publishing Company, 226 pp.
- Josey, S. A., E. C. Kent, and P. K. Taylor, 1998: The Southampton Oceanography Center (SOC) Ocean-Atmosphere Heat, Momentum and Freshwater Flux Atlas. *Southampton Oceanography Centre Rep.* 6, 30 pp.
- Kalnay, E., M. Kanamitsu, R. Kistler, W. Collins, D. Deaven, L. Gandin, M. Iredell, S. Saha, G. White, J. Woollen, Y. Zhu, M. Chelliah, W. Ebisuzaki, W. Higgins, J. Janowiak, K. C. Mo, C. Ropelewski, J. Wang, Leetmaa, R. Reynolds, R. Jenne, and D. Joseph, 1996: The NCEP/NCAR 40-year Reanalysis Project. *Bull. American Meteorol. Soc.*, 77, 437-471.
- Kanamitsu, M., W. Ebisuzaki, J. Woollen, S.-K. Yang, J. J. Hnilo, M. Fiorino, and G. L. Potter, 2002: NCEP-DOE AMIP-II Reanalysis (R-2). *Bull. Amer. Meteor. Soc.*, 83, 1631-1643.
- Kara, A. B., P. A. Rochford, and H. E. Hurlburt, 2003: Mixed layer variability over the global ocean. *J. Geophys. Res.*, 108, 3079, doi:10.1029/2000JC000736.
- Kara, A. B. and H. E. Hurlburt, 2004: A note on the stability-dependent exchange coefficients of air-sea fluxes for use in general circulation models. *J. Atmos. Oceanic Technol.*, In press.
- Klein, S. A., B. J. Soden and N.-C. Lau, 1999: Remote sea surface temperature variations during ENSO: evidence for a tropical atmospheric bridge. *J. Climate*, 12, 917-932.
- Large, W. G., J. C. McWilliams, S. C. Doney, 1994. Oceanic vertical mixing: a review and a model with a non-local boundary layer parameterization. *Rev. Geophys.* 32, 363-403.
- Lee, S.-K. and G. T. Csanady, 1999. Warm water formation and escape in the upper tropical Atlantic Ocean: 1. A literature review. *J. Geophys. Res.*, 104, 29,561-29,571.
- Legeckis, R. and G. Reverdin, 1987: Long waves in the equatorial Atlantic Ocean during 1983. *J. Geophys. Res.*, 92, 2835-2842.
- Levitus, S., T. Boyer, 1994. In: World Ocean Atlas 1994 Volume 4: Temperature. NOAA Atlas NESDIS 4. US Department of Commerce, Washington, DC.
- Levitus, S., R. Burgett, and T. Boyer, 1994. In: World Ocean Atlas 1994 Volume 3: Salinity. NOAA Atlas NESDIS 3. US Department of Commerce, Washington, DC.
- Liu, W. T., K. B. Katsaros, and J. A. Businger, 1979: Bulk parameterization of air-sea exchanges of heat and water vapor including molecular constraints at the interface. *J. Atmos. Sci.*, 36, 1722-1735.
- Lowe, P. R., 1977: An approximating polynomial for the computation of saturation vapor pressure. *J. Appl. Meteorol.*, 16, 100-103.
- Martin, P. J., 1985: Simulation of the mixed layer at OWS November Papa with several models. *J. Geophys. Res.*, 90, 903-9156.
- McCreary, J. P., H. S. Lee, and D. B. Enfield, 1989: The response of the coastal ocean to strong offshore winds: With application to circulations in the Gulfs of Tehuantepec and Papagayo. *J. Mar. Res.*, 47, 81-109.
- McLain, C. R., J. R. Christian, S. R. Signorini, M. R. Lewis, I. Asanuma, D. Turk, and C. Dupouy-Douchement, 2002: Satellite ocean-color observations of the tropical Pacific Ocean. *Deep Sea Res. II*, 49, 2533-2560.
- McPhaden, M. J., 1982: Variability in the central equatorial Indian Ocean. Part II: Oceanic heat and turbulent energy balance. *J. Mar. Res.*, 40, 403-419.

- Mellor, G. L., T., Yamada, , 1982: Development of a turbulence closure model for geophysical fluid problems. *Rev. Geophys. Space Phys.*, 20, 851–875.
- Murtugudde, J. Beauchamp, and A. Busalacchi, 2002: Effects of penetrative radiation on the upper tropical ocean circulation, *J. Climate*, 15, 470-486.
- Oberhuber, J. M., 1988: An atlas based on the COADS data set: The budget of heat, buoyancy and turbulent kinetic energy at the surface of the global ocean. 15,199pp.
- Renfrew, I. A., G. W. K. Moore, P. S. Guest and K. Bumke, 2002: A comparison of surface layer and surface turbulent flux observations over the Labrador Sea with ECMWF analysis and NCEP reanalysis. *J. Phys. Oceanogr.*, 32, 383-400.
- Simmonds, I., and M. Dix, 1989: The use of mean atmospheric parameters in the calculation of modeled mean surface heat fluxes over the world's oceans. *J. Phys. Oceanogr.*, 19, 205-215.
- Smith, S. D. 1988: Coefficients for sea surface wind stress, heat flux, and wind profiles as a function of wind speed and temperature. *J. Geophys. Res.*, 93, 15,467-15,472.
- Smith, S. R., D. M. Legler, and K. V. Verzone, 1999: Quantifying uncertainties in NCEP reanalysis using high quality research vessel observations. *Proc. Second Int. Conf. on Reanalysis*, Reading, United Kingdom, ECMWF, 133-136.
- Sun, B., L. Yu, and R. A. Weller, 2003: Comparisons of surface meteorology and turbulent heat fluxes over the Atlantic: NWP model analysis versus moored buoy observations. *J. Climate*, 16, 679-695.
- Toole, J. M., H.-M. Zhang, and M. J. Caruso, 2004: Time-dependent internal energy budgets of the tropical warm water pools. *J. Climate*, 17, 1398-1410.
- Wang, C., 2002: Atlantic climate variability and its associated atmospheric circulation cells. *J. Climate*, 15, 1516-1536.
- Wang, C., 2004: ENSO, Atlantic climate variability, and the Walker and Hadley circulations. In: *The Hadley Circulation: Present, Past, and Future*. H. F. Diaz and R. S. Bradley, Eds., Cambridge University Press, in press.
- Wang, C. and D. B. Enfield, 2001: The Tropical Western Hemisphere warm pool. *Geophys. Res. Lett.*, 28, 1635-1638.
- Wang, C. and D. B. Enfield, 2003: A further study of the tropical Western Hemisphere warm pool. *J. Climate*, 16, 1476-1493.
- Wang, D., W. G. Large, and J. C. McWilliams, 1996: Large-eddy simulation of the equatorial ocean boundary layer: Diurnal cycling, eddy viscosity, and horizontal rotation. *J. Geophys. Res.*, 101, 3649-3662.
- Wang, W., and M. J. McPhaden, 1999: The surface-layer heat balance in the equatorial Pacific Ocean. Part I: Mean seasonal cycle. *J. Phys. Oceanogr.*, 29, 1812-1831.
- Vialard, J., C. Menkes, J.-P. Boulanger, P. Delecluse, E. Guilyardi, M. J. McPhaden and G. Madec, 2001: A model study of oceanic mechanisms affecting equatorial Pacific sea surface temperature during the 1997-98 El Nino. *J. Phys. Oceanogr.*, 31, 1649-1675.
- Weingartner, T. J., and R. H. Weisberg, 1991: A description of the annual cycle in seas surface temperature and upper ocean heat in the equatorial Atlantic. *J. Phys. Oceanogr.*, 21, 83-96.
- Zeng, X., M. Zhao, and R. E. Dickinson, 1998. Intercomparison of bulk aerodynamic algorithms for the computation of sea surface fluxes using TOGA COARE and TAO data. *J. Climate*, 11, 2628-2644.
- Zhang, G. J., 1995: Use of monthly mean data to compute surface turbulent fluxes in the tropical Pacific. *J. Climate*, 8, 3084-3090.

- Zhang, G. J, 1997: A further study on estimating surface evaporation using monthly mean data: comparison of bulk formulations. *J. Climate*, 10, 1592-1600.
- Zhang, J., R. W. Schmitt, and R. X. Huang, 1998: Sensitivity of the GFDL Modular Ocean Model to parameterization of double-diffusive processes. *J. Phys. Oceanogr.*, 28, 589-605.

Table 1. The surface forcing, mixed layer model, and the light attenuation depth used for the sixteen major experiments.

Experiments	Surface forcing	Mixing model	Attenuation Depth
SHC-KPP	Southampton constrained	KPP ($Ric = 0.30$; $Ri_0 = 0.70$)	KPAR ⁻¹
OBH-KPP	Oberhuber	KPP ($Ric = 0.30$; $Ri_0 = 0.70$)	KPAR ⁻¹
SHU-KPP	Southampton unconstrained	KPP ($Ric = 0.30$; $Ri_0 = 0.70$)	KPAR ⁻¹
DSU-KPP	da Silva unconstrained	KPP ($Ric = 0.30$; $Ri_0 = 0.70$)	KPAR ⁻¹
NCEP1-KPP	NCEP reanalysis-1 (1949-2003)	KPP ($Ric = 0.30$; $Ri_0 = 0.70$)	KPAR ⁻¹
NCEP2-KPP	NCEP reanalysis-2 (1979-2002)	KPP ($Ric = 0.30$; $Ri_0 = 0.70$)	KPAR ⁻¹
ERA15-KPP	15-yrs ECMWF reanalysis (1979-1993)	KPP ($Ric = 0.30$; $Ri_0 = 0.70$)	KPAR ⁻¹
ERA40-KPP	40-yrs ECMWF reanalysis (1958-2001)	KPP ($Ric = 0.30$; $Ri_0 = 0.70$)	KPAR ⁻¹
SHC-JW1-KPP	Southampton constrained	KPP ($Ric = 0.30$; $Ri_0 = 0.70$)	23m
SHC-JW3-KPP	Southampton constrained	KPP ($Ric = 0.30$; $Ri_0 = 0.70$)	17m
SHC-KPP-a	Southampton constrained	KPP ($Ric = 1.00$; $Ri_0 = 1.00$)	KPAR ⁻¹
SHC-KPP-b	Southampton constrained	KPP ($Ric = 1.00$; $Ri_0 = 0.25$)	KPAR ⁻¹
SHC-KPP-c	Southampton constrained	KPP ($Ric = 0.25$; $Ri_0 = 1.00$)	KPAR ⁻¹
SHC-KPP-d	Southampton constrained	KPP ($Ric = 0.25$; $Ri_0 = 0.25$)	KPAR ⁻¹
SHC-KPP-e	Southampton constrained	KPP ($Ric = 0.30$; $Ri_0 = 0.70$; diffusivity due to internal wave breaking turned off)	KPAR ⁻¹
SHC-GISS	Southampton constrained	GISS (Goddard Inst. Space Studies)	KPAR ⁻¹

Table 2. Performance of HYCOM experiments under the sixteen different conditions, measured by 95% confidence limits of the mean SST errors ($^{\circ}\text{C}$). Note that the mean errors for the four WHWP sub-regions are obtained exclusively for the warm pool SST ($\text{SST} \geq 27.5^{\circ}\text{C}$).

Experiments	ENP (APR–JUN)	GoM (JUL–SEP)	CBN (AUG–OCT)	EQA (MAR–MAY)	Total (JAN–DEC)
SHC-KPP	0.16 ± 0.02	-0.01 ± 0.01	-0.08 ± 0.01	-0.39 ± 0.02	-0.11 ± 0.01
OBH-KPP	0.22 ± 0.03	-0.17 ± 0.01	-0.19 ± 0.02	-0.22 ± 0.03	-0.13 ± 0.01
SHU-KPP	1.29 ± 0.02	0.98 ± 0.01	0.91 ± 0.01	0.64 ± 0.02	0.92 ± 0.01
DSU-KPP	1.49 ± 0.03	1.10 ± 0.01	1.03 ± 0.01	0.88 ± 0.02	1.10 ± 0.01
NCEP1-KPP	0.60 ± 0.04	-0.29 ± 0.02	-0.32 ± 0.02	-0.15 ± 0.02	-0.01 ± 0.01
NCEP2-KPP	-0.24 ± 0.04	-0.07 ± 0.02	-0.25 ± 0.01	-1.19 ± 0.03	-0.41 ± 0.02
ERA15-KPP	-0.15 ± 0.04	-1.28 ± 0.02	-1.45 ± 0.02	-1.60 ± 0.03	-0.98 ± 0.02
ERA40-KPP	0.41 ± 0.03	-0.69 ± 0.02	-0.74 ± 0.01	-0.67 ± 0.02	-0.40 ± 0.01
SHC-JW1-KPP	-0.25 ± 0.02	-0.25 ± 0.01	-0.29 ± 0.01	-0.52 ± 0.02	-0.33 ± 0.01
SHC-JW3-KPP	-0.02 ± 0.02	-0.08 ± 0.01	-0.14 ± 0.01	-0.45 ± 0.02	-0.20 ± 0.01
SHC-KPP-a	0.14 ± 0.02	-0.03 ± 0.01	-0.10 ± 0.01	-0.37 ± 0.02	-0.11 ± 0.01
SHC-KPP-b	0.15 ± 0.02	-0.01 ± 0.01	-0.08 ± 0.01	-0.40 ± 0.02	-0.11 ± 0.01
SHC-KPP-c	0.17 ± 0.02	-0.01 ± 0.01	-0.08 ± 0.01	-0.38 ± 0.02	-0.11 ± 0.01
SHC-KPP-d	0.15 ± 0.02	-0.00 ± 0.01	-0.08 ± 0.01	-0.43 ± 0.02	-0.12 ± 0.01
SHC-KPP-e	0.30 ± 0.02	0.07 ± 0.01	-0.01 ± 0.01	-0.27 ± 0.02	-0.01 ± 0.01
SHC-GISS	0.25 ± 0.02	0.06 ± 0.01	-0.06 ± 0.01	-0.38 ± 0.03	-0.06 ± 0.01

Table 3. Performance of HYCOM experiments under the sixteen different conditions, measured by 95% confidence limits of SST pattern correlations. Note that the pattern correlations for the four WHWP sub-regions are obtained exclusively for the warm pool SST ($SST \geq 27.5^{\circ}C$).

Experiments	ENP (APR–JUN)	GoM (JUL–SEP)	CBN (AUG–OCT)	EQA (MAR–MAY)	Total (JAN–DEC)
SHC-KPP	0.85 ± 0.06	0.90 ± 0.04	0.88 ± 0.03	0.67 ± 0.04	0.78 ± 0.02
OBH-KPP	0.76 ± 0.06	0.86 ± 0.04	0.80 ± 0.03	0.70 ± 0.04	0.70 ± 0.02
SHU-KPP	0.86 ± 0.06	0.88 ± 0.04	0.84 ± 0.04	0.66 ± 0.04	0.77 ± 0.02
DSU-KPP	0.87 ± 0.05	0.88 ± 0.04	0.84 ± 0.04	0.76 ± 0.04	0.81 ± 0.02
NCEP1-KPP	0.57 ± 0.06	0.68 ± 0.04	0.56 ± 0.03	0.62 ± 0.04	0.54 ± 0.02
NCEP2-KPP	0.65 ± 0.06	0.79 ± 0.04	0.77 ± 0.03	0.36 ± 0.04	0.53 ± 0.02
ERA15-KPP	0.67 ± 0.05	0.66 ± 0.04	0.66 ± 0.04	0.54 ± 0.04	0.54 ± 0.02
ERA40-KPP	0.65 ± 0.05	0.73 ± 0.03	0.65 ± 0.03	0.46 ± 0.04	0.57 ± 0.02
SHC-JW1-KPP	0.80 ± 0.05	0.90 ± 0.04	0.89 ± 0.03	0.66 ± 0.04	0.78 ± 0.02
SHC-JW3-KPP	0.84 ± 0.06	0.90 ± 0.04	0.89 ± 0.04	0.66 ± 0.04	0.78 ± 0.02
SHC-KPP-a	0.84 ± 0.06	0.90 ± 0.03	0.88 ± 0.04	0.71 ± 0.04	0.79 ± 0.02
SHC-KPP-b	0.85 ± 0.06	0.90 ± 0.04	0.88 ± 0.04	0.61 ± 0.04	0.76 ± 0.02
SHC-KPP-c	0.84 ± 0.06	0.90 ± 0.04	0.88 ± 0.04	0.69 ± 0.04	0.78 ± 0.02
SHC-KPP-d	0.85 ± 0.06	0.89 ± 0.04	0.88 ± 0.03	0.58 ± 0.04	0.75 ± 0.02
SHC-KPP-e	0.83 ± 0.06	0.89 ± 0.04	0.86 ± 0.03	0.70 ± 0.04	0.78 ± 0.02
SHC-GISS	0.85 ± 0.05	0.87 ± 0.04	0.86 ± 0.03	0.62 ± 0.04	0.74 ± 0.02

Figure captions

Figure 1. The model grid structure in the eastern tropical Pacific and the tropical Atlantic analysis domain (uniform 1° in zonal and variable in meridional direction; 0.5° at the equator increasing linearly to 1° at 40° latitude and 1° pole ward of 40°). The locations of the four subregions of the WHWP are also shown. Note that the entire model domain contains both Pacific and Atlantic Oceans between 113°E and 20°E , bounded north and south by 35°S and 65°N , respectively.

Figure 2. The annual cycles of the net heat flux into the four WHWP regions obtained from the eight heat flux climatologies. The values used in the plots are obtained by computing the spatial average over a rectangular box centered near each WHWP subregion. The left column is from the original datasets, and the right column is obtained by evaluating the turbulent heat fluxes using the HYCOM bulk formulas and the SST from World Ocean Atlas 2001 (WOA01) climatology (Conkright et al., 2002).

Figure 3. Simulated (SHC-KPP, OBH-KPP, SHU-KPP, DSU-KPP, NCEP1-KPP, NCEP2-KPP, ERA15-KPP and ERA40-KPP) versus observed (WOA01: first row) WHWP SST in February, April, June, August and October. The unit is in $^\circ\text{C}$.

Figure 4. Linear regression of the model SST bias and the net surface heat flux from the eight experiments (SHC-KPP, OBH-KPP, SHU-KPP, DSU-KPP, NCEP1-KPP, NCEP2-KPP, ERA15-KPP and ERA40-KPP) grouped for each WHWP sub-region.

Figure 5. Annual cycles of the simulated (SHC-KPP, OBH-KPP, SHU-KPP, DSU-KPP, NCEP1-KPP, NCEP2-KPP, ERA15-KPP and ERA40-KPP) versus observed (WOA01: first row) subsurface temperature profiles, near the center of the four WHWP subregions. The unit is in $^\circ\text{C}$.

Figure 6. Simulated annual cycle of the volume-averaged temperature (first row) and slab heat budget terms (Q_{STR} , $Q_{NET} + Q_{SWP}$, and $Q_{ADV} + Q_{DIF}$) of the ENP obtained the eight experiments (SHC-KPP, OBH-KPP, SHU-KPP, DSU-KPP, NCEP1-KPP, NCEP2-KPP, ERA15-KPP and ERA40-KPP). The observed volume-averaged temperature and the storage rate (Q_{STR}) from the WOA01 are plotted in thick solid lines. The depth of the slab is taken as 20m, which is the approximate depth of 27.5°C for the ENP.

Figure 7. Same as Figure 6 except for the GoM slab. The depth of the GoM slab is taken as 20m.

Figure 8. Same as Figure 6 except for the CBN slab. The depth of the CBN slab is taken as 40m.

Figure 9. Same as Figure 6 except for the EQA slab. The depth of the EQA slab is taken as 30m.

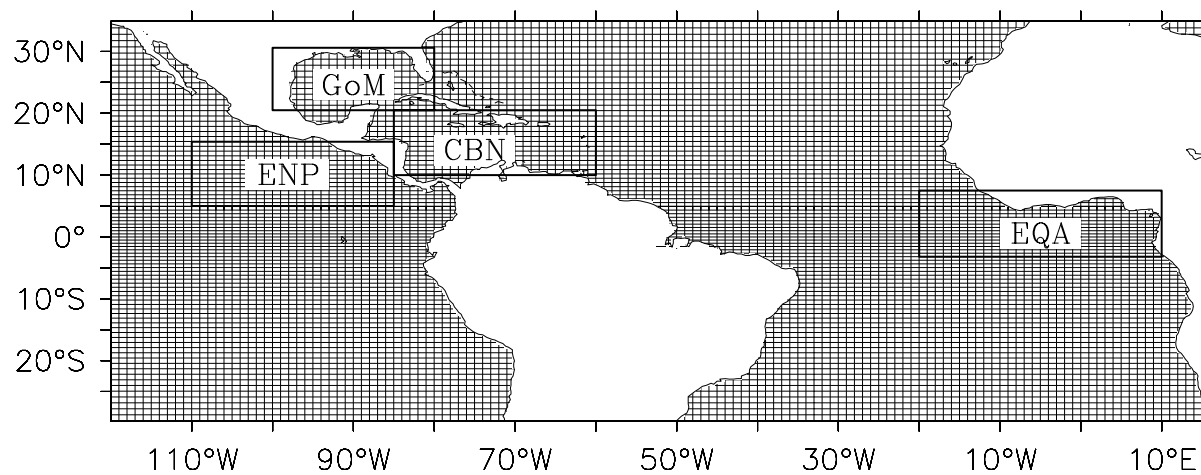


Figure 1

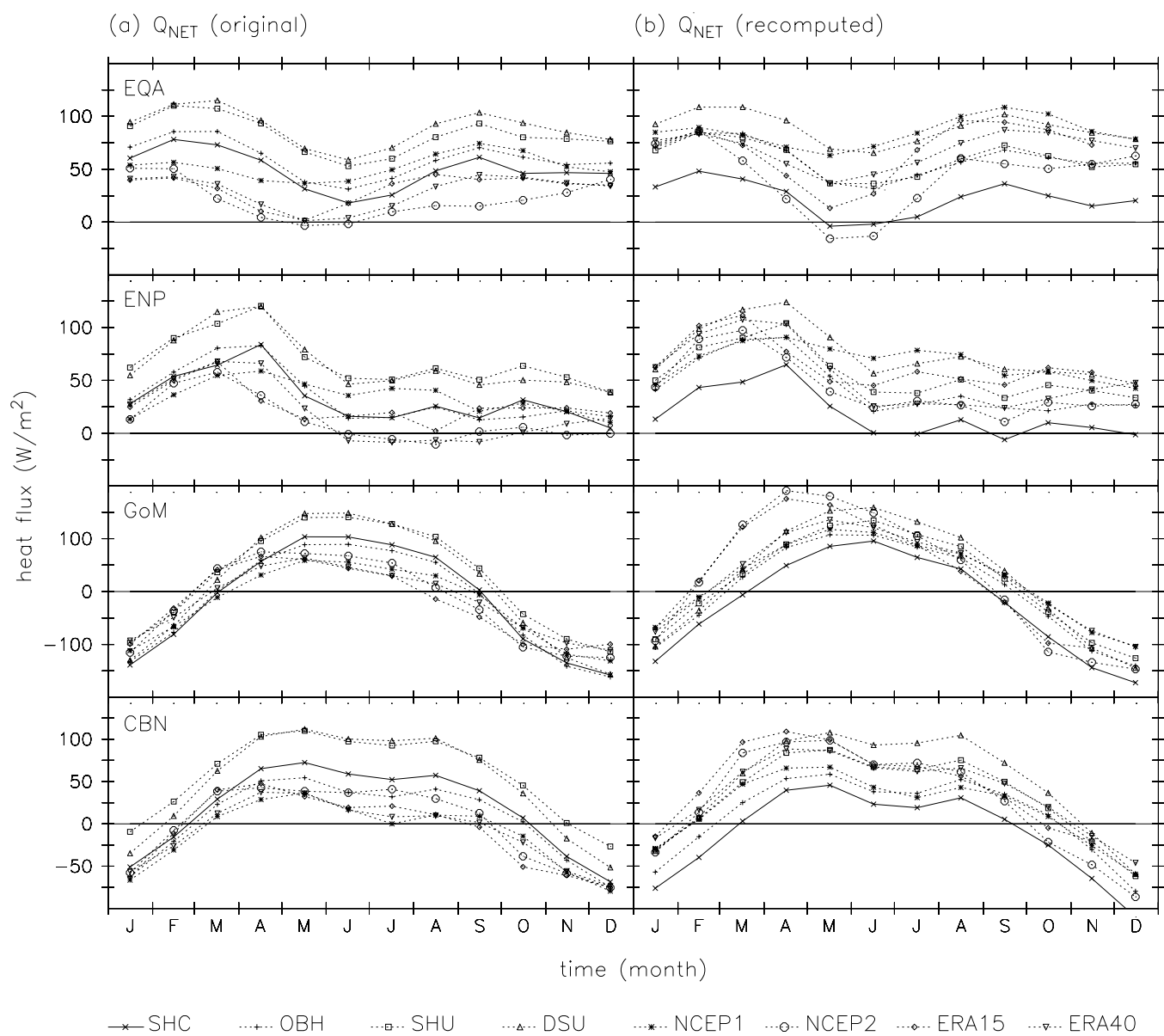


Figure 2

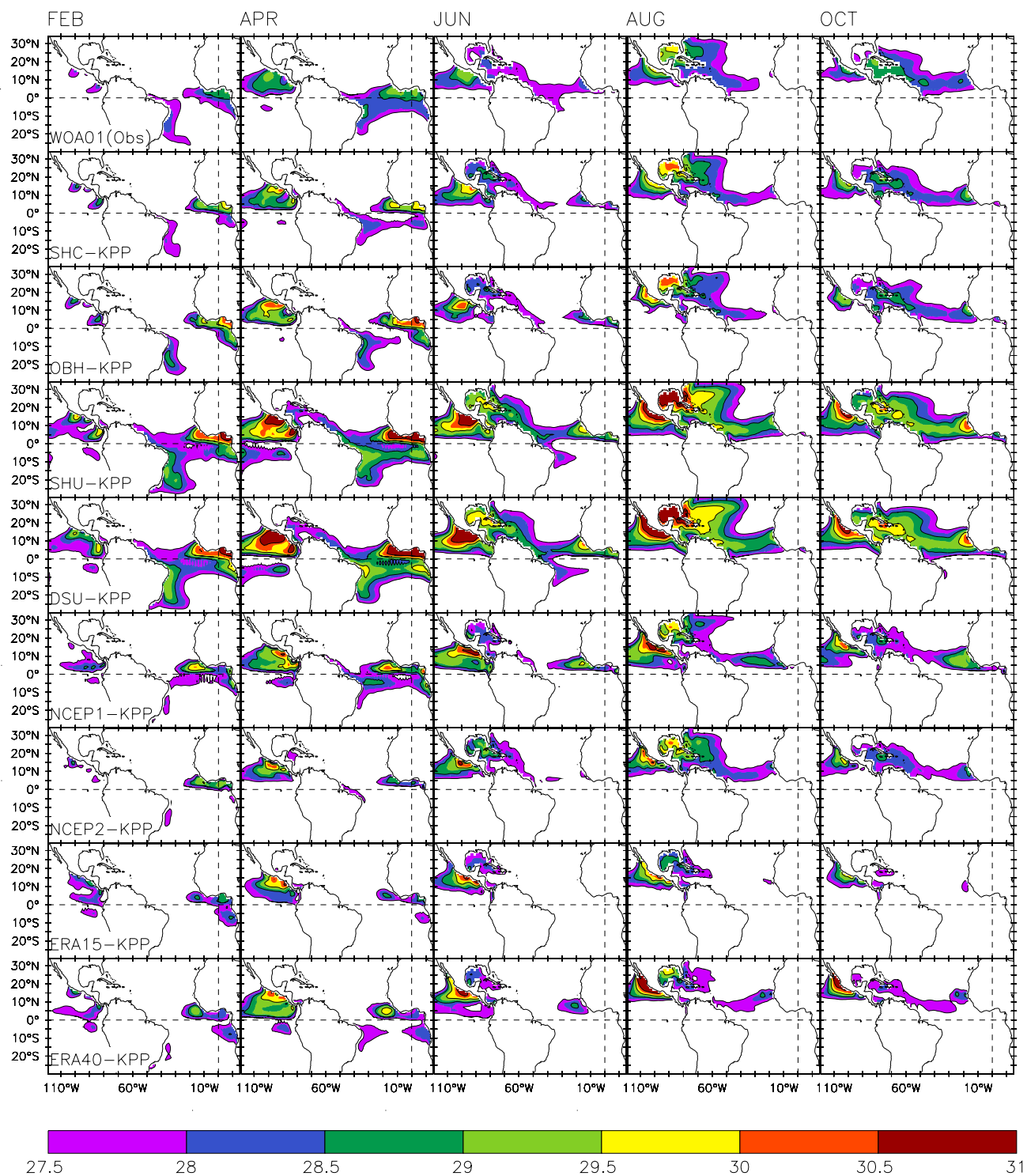


Figure 3

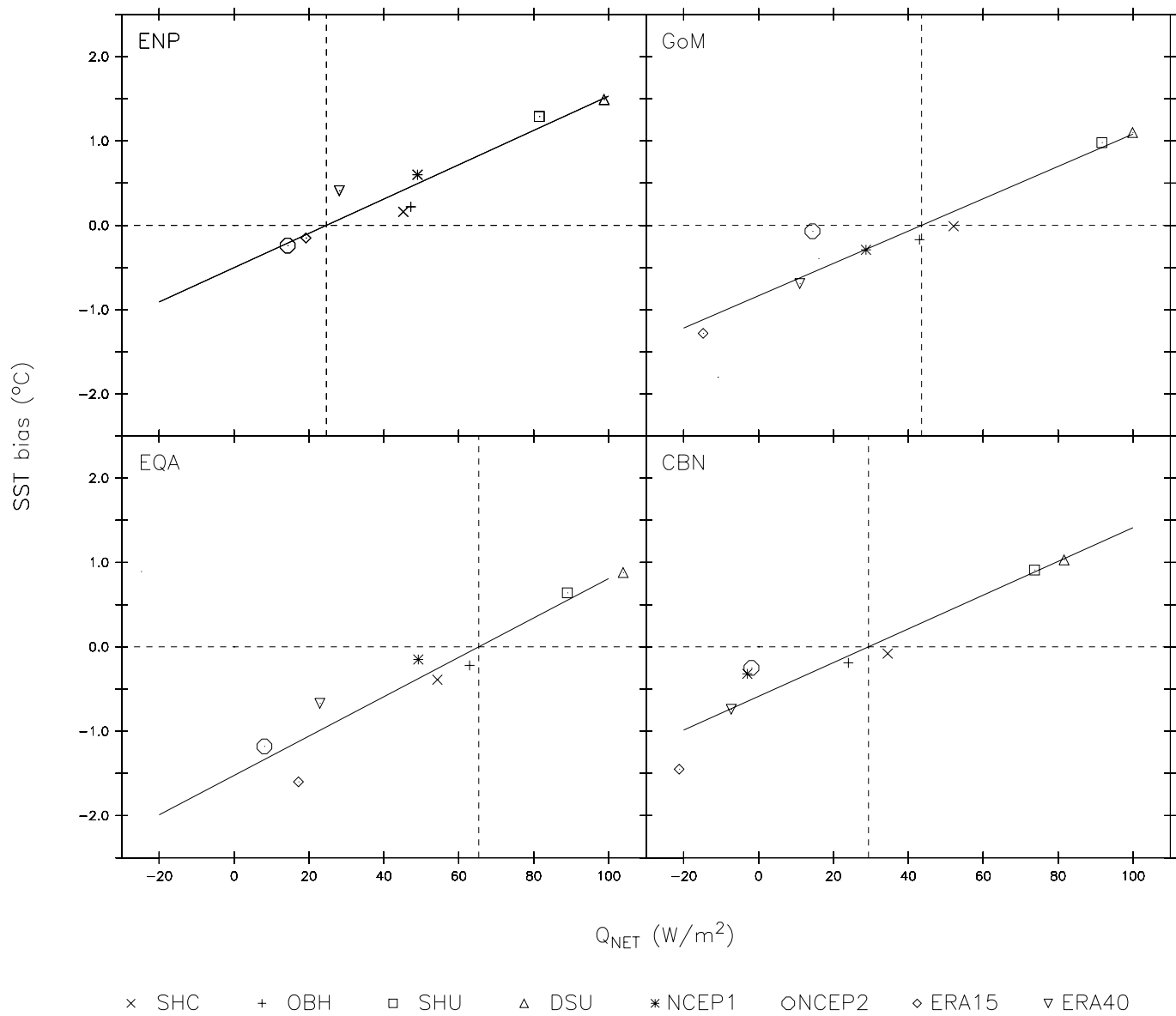


Figure 4

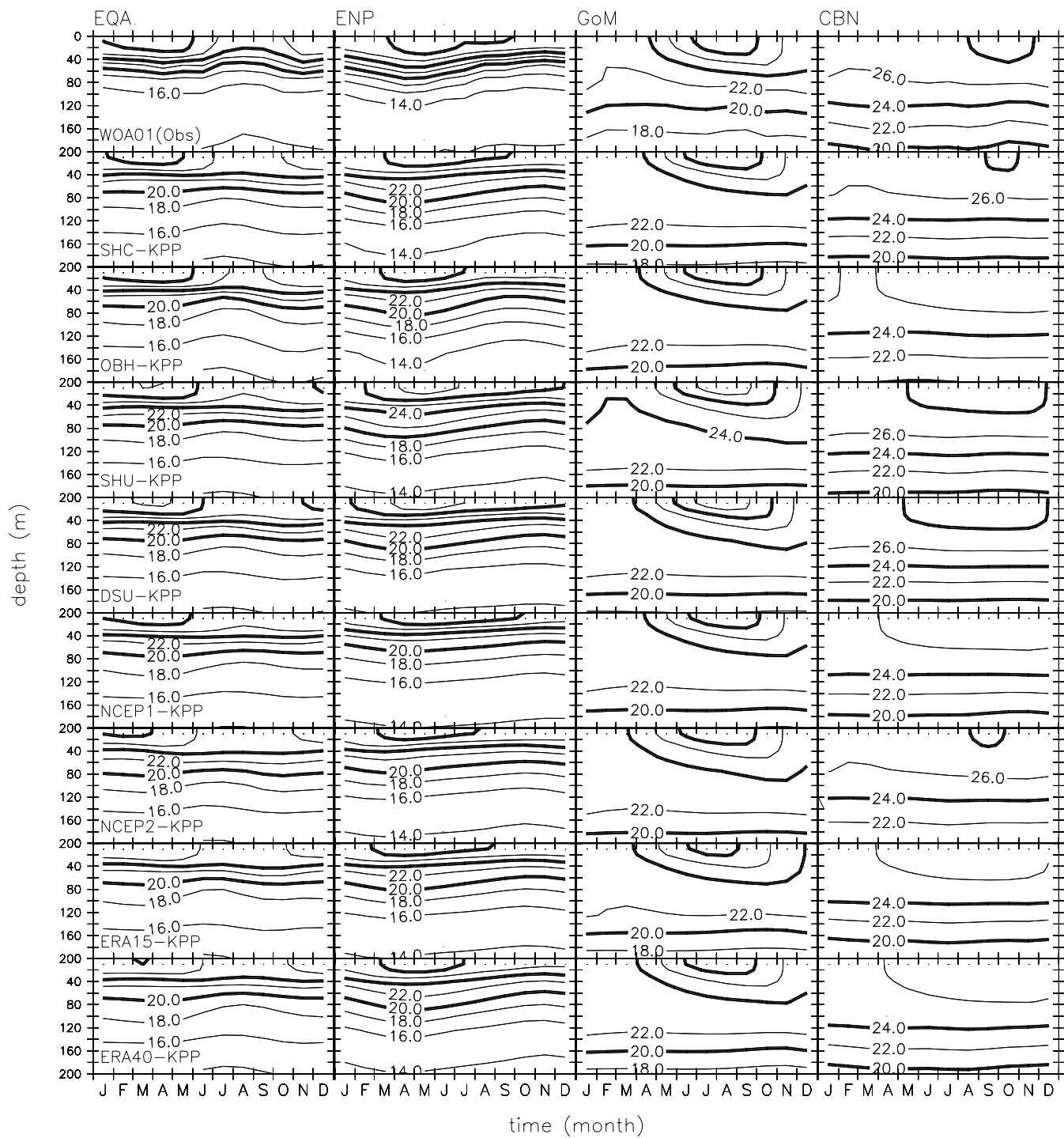


Figure 5

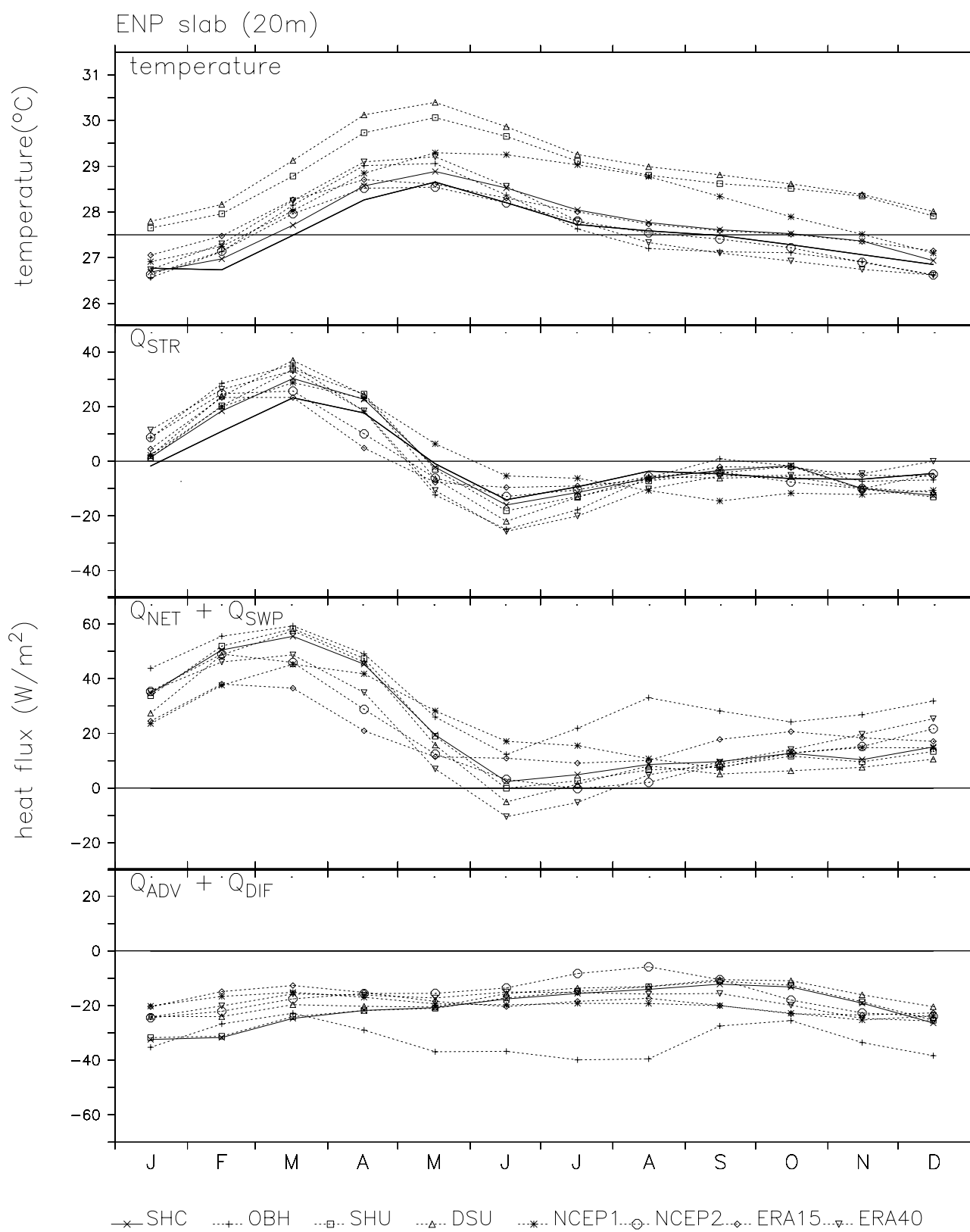


Figure 6

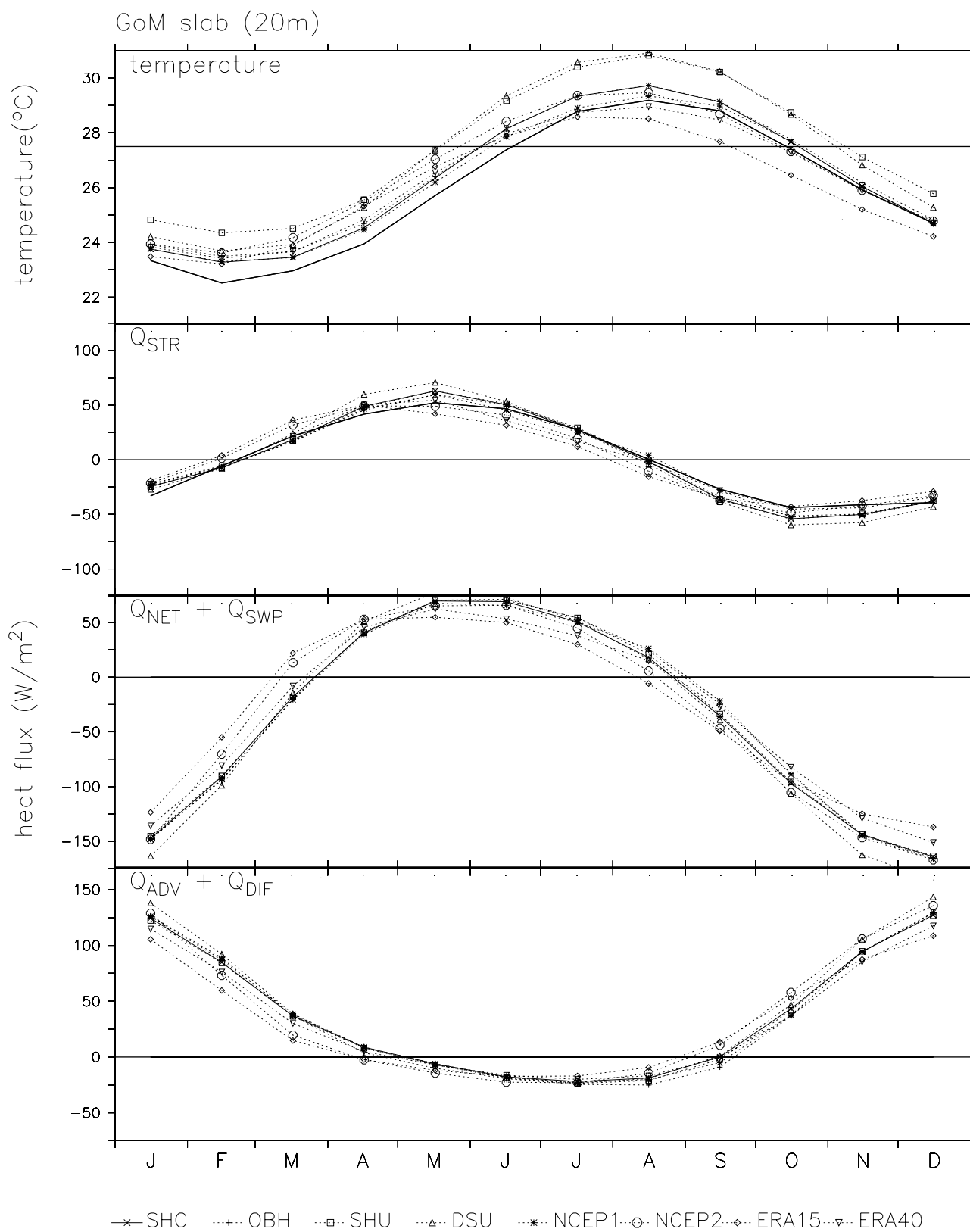


Figure 7

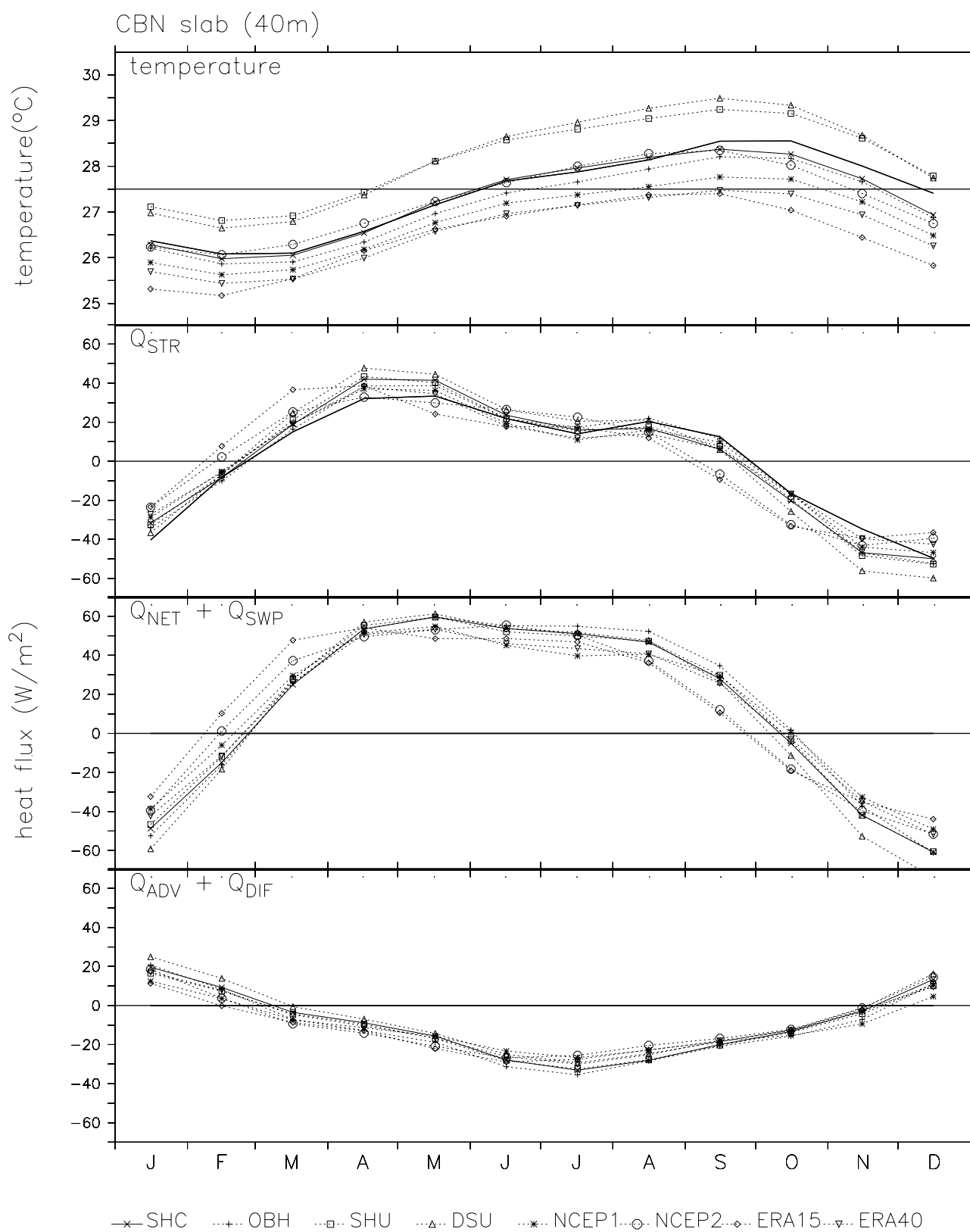


Figure 8

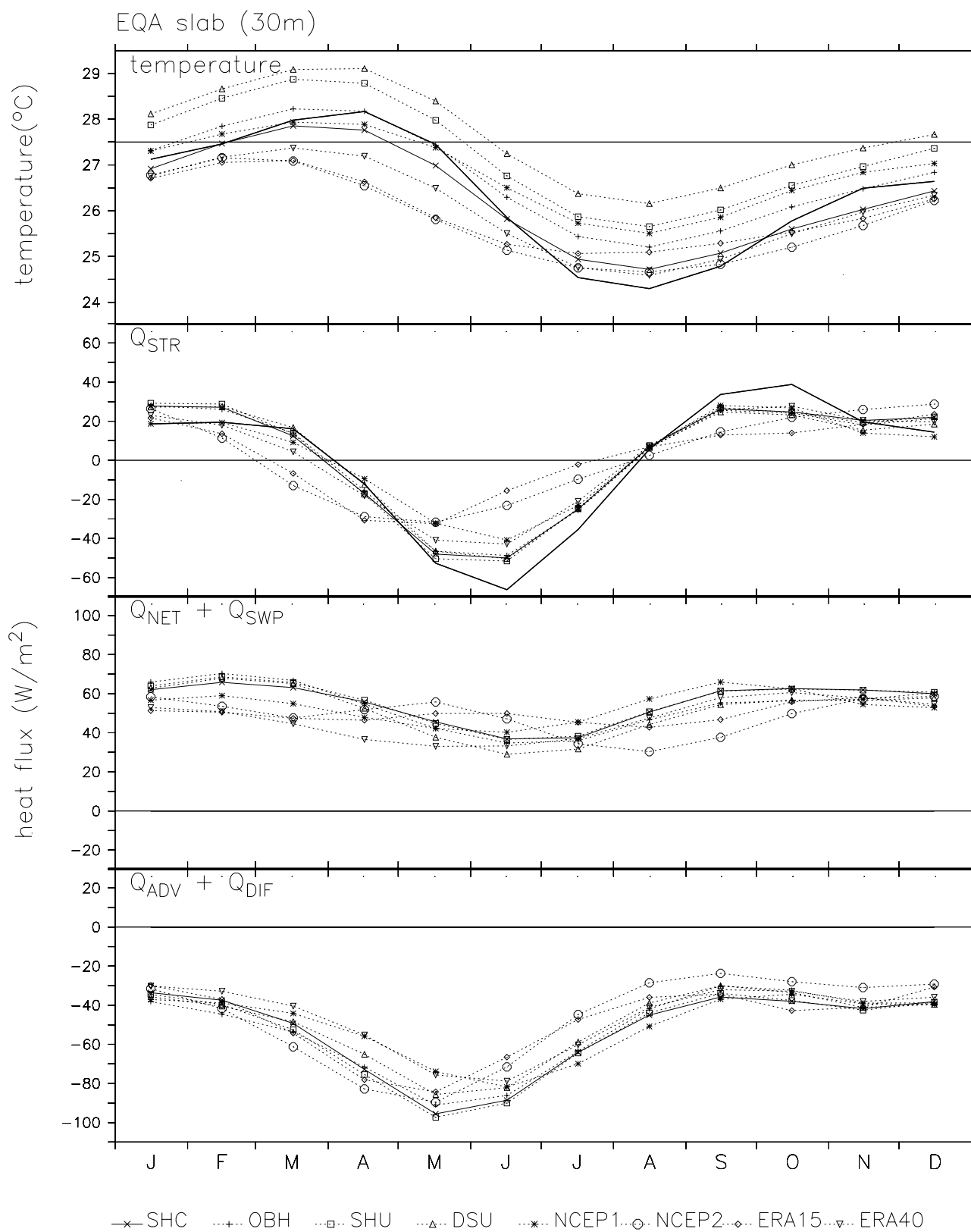


Figure 9